

# Diffuse-interface blended method for the imposition of physical boundaries in two-fluid flows

Tanyakarn Treeratanaphitak<sup>a,\*</sup>, Nasser Mohieddin Abukhdeir<sup>a,b</sup>

<sup>a</sup>*Department of Chemical Engineering, University of Waterloo, 200 University Avenue West  
Waterloo, N2L 3G1, ON, Canada*

<sup>b</sup>*Department of Physics & Astronomy, University of Waterloo, 200 University Avenue West  
Waterloo, N2L 3G1, ON, Canada*

---

## Abstract

Multiphase flows are commonly found in chemical engineering processes such as distillation columns, bubble columns, fluidized beds and heat exchangers. Physical boundaries in numerical simulations of multiphase flows are generally defined by a mesh that conforms to the physical boundaries of the system. Depending on the complexity of the physical system, generating the conformal mesh can be time-consuming and the resulting mesh could potentially contain a large number of skewed elements, which is undesirable. The diffuse-interface approach allows for a structured mesh to be used while still capturing the desired solid-fluid boundaries. In this work, a diffuse-interface method for the imposition of physical boundaries is developed for two-fluid incompressible flow systems. The diffuse-interface is used to define the physical boundaries and the boundary conditions are imposed by blending the conservation equations from the two-fluid model with that of the solid. The results from the diffuse-interface method and mesh-defined boundaries are found to be in good agreement at small diffuse-interface widths.

*Keywords:* two-phase flow, computational fluid dynamics, two-fluid model, diffuse-interface

---

## Nomenclature

$\alpha$	Time-averaged local phase fraction
$\Delta t$	Time step
$\epsilon$	Diffuse-interface width parameter
$\eta$	Diffuse-interface width

---

\*Corresponding author

*Email addresses:* [ttreerat@uwaterloo.ca](mailto:ttreerat@uwaterloo.ca) (Tanyakarn Treeratanaphitak),  
[nmabukhdeir@uwaterloo.ca](mailto:nmabukhdeir@uwaterloo.ca) (Nasser Mohieddin Abukhdeir)

*URL:* <http://uwaterloo.ca/comphys> (Nasser Mohieddin Abukhdeir)

$\Gamma$	Simulation domain boundary
$\langle \cdot, \cdot \rangle$	Inner product
$\Omega$	Simulation domain
$\rho$	Density
$\tilde{\mathbf{x}}_c$	Scaled diffuse-interface position vector
$\mathbf{v}$	Velocity vector
$\mathbf{x}$	Position vector
$a_j$	Backward-differentiation coefficient
$b_j$	Adams-Bashforth coefficient
$C_D$	Drag coefficient
$C_P$	Interfacial pressure coefficient
$d$	Diameter
$Eu$	Euler number
$Fr$	Froude number
$r_d$	Volume to projected area ratio
$Re$	Reynolds number
$t$	Time

## 1. Introduction

Industrial chemical engineering processes such as bubble columns (Jakobsen et al., 2005; Joshi, 2001; Ekambara et al., 2005; Krishna and van Baten, 2001), reactors (Becker et al., 1994; Sokolichin and Eigenberger, 1994) and separators (Lane et al., 2016) involve two or more fluids. To better design and operate these processes, an understanding of the hydrodynamics of the system is essential. An emergent tool in studying multiphase flow systems that is becoming readily accessible to researchers is computational fluid dynamics (CFD) simulations. CFD simulations of multiphase flow systems enable researchers to explore different combinations of operating conditions and prototype designs without the cost and safety issues incurred by experimental design and pilot studies, which is extremely beneficial in the design and optimization of process equipment.

A crucial aspect in the use of CFD for design and optimization of process equipment is the specification of internal physical features, which can have highly complex shapes. These features need to be specified as physical boundaries in the simulation, which can be achieved by either using a conformal mesh or an embedded domain method. With a conformal mesh, the geometry is defined such that once generated, the mesh surfaces correspond to the physical boundaries. This process can be tedious, time-consuming and have detrimental numerical effects (computational complexity and numerical stability) for complicated geometries. Additionally, if the internal features are changed, which is likely the case during the design and optimization process, the mesh will also have to change, thus requiring the mesh to be regenerated. In the case of moving mesh problems, methods like the arbitrary Lagrangian-Eulerian (ALE) method (Donea et al., 2004) are used, but ALE requires the mesh to be deformed as the boundary moves.

Instead of using a conformal mesh, the physical boundaries can be “embedded” in the problem using methods such as fictitious domain (Glowinski et al., 1999), immersed boundary (Mittal and Iaccarino, 2005; Sotiropoulos and Yang, 2014; Griffith and Patankar, 2020) and diffuse domain/interface (Ramière et al., 2007; Li et al., 2009; Aland et al., 2010; Schlottbom, 2016; Nguyen et al., 2018) methods. The physical boundaries are defined in the embedded domain method through the use of a level-set function, a phase-field, *etc.* Since the physical boundaries are not explicitly defined by the domain mesh, it is not required to conform to the physical boundaries and a simple structured mesh can be used. This has the benefit of avoiding skewed elements that are detrimental to the numerical accuracy of the solution. The ease in which the internal features can be changed during simulation is highly beneficial when optimizing a design since the field that describes the boundaries can directly be modified by the optimization scheme.

The immersed boundary (IB) method has been extensively used to impose solid boundaries in single-phase flow. Single-phase immersed boundary studies are reviewed in Mittal and Iaccarino (2005); Sotiropoulos and Yang (2014); Griffith and Patankar (2020). The method has also been used to impose solid boundary conditions in multiphase flow where the flow is modeled using interface-capturing methods (Shen and Chan, 2008, 2010, 2011; Zhang et al., 2013, 2014; Gsell et al., 2016; Yang and Stern, 2009; Son, 2005; Arienti and Sussman, 2014; Patel et al., 2017; Washino et al., 2011; Sun and Sakai, 2015; Suh and Son, 2009; Horgue et al., 2014; Vincent et al., 2011). The use of interface-capturing methods allows for the solid boundary to be accounted for using the same methods as single-phase IB. Applications of IB with interface-capturing include wave propagation (Shen and Chan, 2008, 2010, 2011; Zhang et al., 2013, 2014; Gsell et al., 2016; Yang and Stern, 2009), injectors (Suh and Son, 2009; Arienti and Sussman, 2014), porous media (Patel et al., 2017), hydroplaning (Vincent et al., 2011) and capillary flow (Horgue et al., 2014). The use of interface-capturing methods severely limit the flow regimes that can be modeled since every interface in the domain is resolved.

Physical boundaries that are defined using fictitious domain and immersed boundary methods are generally sharp boundaries whose effect may be approximated through the distribution of the boundary over several mesh elements. This requires the solution

field to be interpolated from the physical boundary to the nearest neighboring node/cell (Patel and Natarajan, 2018). Special consideration must also be paid when handling mesh elements that are cut by the embedded boundaries (Nguyen et al., 2018). The diffuse domain/interface method defines the physical boundaries using a phase-field. For example, the phase-field can vary between zero and one (Nguyen et al., 2018):

$$\phi = \begin{cases} 1, & \text{physical domain,} \\ 0, & \text{otherwise,} \end{cases} \quad (1)$$

where  $\phi$  is the phase-field. The diffuse-interface method has been extensively used to model gas-liquid and liquid-liquid multiphase flows (Abels et al., 2012, 2017; Ding et al., 2007; Jacqmin, 1999; Liu et al., 2015; Shen and Yang, 2010; Sun and Beckermann, 2007; Takada et al., 2006; Anderson et al., 1998). Additionally, the diffuse-interface method has been used to impose solid boundaries in simulations with interface-capturing (Patel and Natarajan, 2018) and interface-resolution (Aland et al., 2010). This method does not require the solution to be interpolated at every time step since the phase-field ensures the smooth transition from the fluid to the solid phase. The boundary normal vector is computed from the gradient of the phase-field, aiding in the imposition of Neumann boundary conditions. Based on these factors, the diffuse-interface method is an attractive approach in imposing physical boundaries in simulations involving multiphase flow.

In this work, a diffuse solid-fluid interface method for imposing solid boundaries in dispersed multiphase flows is presented. The multiphase fluid is modeled using the two-fluid model (Ishii and Hibiki, 2011) where the fluids are treated as inter-penetrating continua. In past work, the multiphase fluid flow regime is restricted by the computational cost of interface-capturing methods and simulations of industrial-scale bubbly flow regimes are not feasible. The use of the two-fluid model with the diffuse-interface method allows for bubbly flow to be modeled without the need for remeshing if the solid boundary is changed. The diffuse solid-fluid interface method is used to model two-dimensional bubbly flow in a rectangular channel and two-dimensional bubbly flow past a stationary cylinder. The results are validated by comparison with simulation results from using boundary-conformal meshes.

The paper is organized as follows: Section 2 – background on the two-fluid model equations, Section 3 – presentation of the diffuse-interface method developed in this work and the numerical method used to solve the governing equations, Section 4 – simulation results on the effect of interface length-scale and function and Section 5 – conclusions.

## 2. Two-Fluid Model

Dispersed gas-liquid flows are modeled using the two-fluid model, where each phase is considered to be a continuous fluid (Ishii and Hibiki, 2011). The instantaneous behavior of the fluid is averaged over time and phase fractions are used to indicate the



spatially-varying composition of the multiphase fluid. Each of the fluids has its own set of governing equations and the interaction between the fluids is accounted for through constitutive interphase momentum transfer relationships. The governing equations of the two-fluid model are given as (Ishii and Hibiki, 2011):

$$\frac{\partial(\alpha_q \rho_q)}{\partial t} + \nabla \cdot (\alpha_q \rho_q \mathbf{v}_q) = 0, \quad (2a)$$

$$\begin{aligned} \frac{\partial(\alpha_q \rho_q \mathbf{v}_q)}{\partial t} + \nabla \cdot (\alpha_q \rho_q \mathbf{v}_q \mathbf{v}_q) = & -\nabla(\alpha_q P_q) + \nabla \cdot (\alpha_q \boldsymbol{\tau}_q) + \alpha_q \rho_q \mathbf{g}_q \\ & + \mathbf{M}_q + P_{q,i} \nabla \alpha_q - \nabla \alpha_q \cdot \boldsymbol{\tau}_{q,i}, \end{aligned} \quad (2b)$$

where  $\mathbf{v}_q$  is the phasic velocity,  $\rho_q$  is the phasic density,  $\alpha_q$  is the phase fraction of phase  $q$ ,  $P_q$  is the phasic pressure,  $\boldsymbol{\tau}_q$  is the phasic viscous stress tensor,  $\mathbf{g}_q$  is the phasic gravitational force,  $\mathbf{M}_q$  is the momentum exchange term and the subscript  $i$  denote interfacial quantities.

The interphase momentum transfer term can include contributions from various modes of transfer including drag, lift, virtual mass and wall lubrication (Ishii and Hibiki, 2011; Lahey Jr. and Drew, 2001; Antal et al., 1991). Drag is the largest contributor to the momentum exchange in two-phase flow (Weller, 2005). It is due to the pressure imbalance and shear forces at the gas-liquid interface. The drag force for the continuous phase,  $c$ , due to the movement of the dispersed phase,  $d$ , is given as (Ishii and Hibiki, 2011):

$$\mathbf{M}_{c,drag} = \frac{1}{2} \rho_c \alpha_d \frac{C_D}{r_d} \|\mathbf{v}_r\| \mathbf{v}_r, \quad (3)$$

where  $r_d$  is the ratio of the volume to projected area of the bubble/particle,  $C_D$  is the drag coefficient and  $\mathbf{v}_r$  is the relative velocity between the dispersed and continuous phases,  $\mathbf{v}_r = \mathbf{v}_d - \mathbf{v}_c$ . In spherical bubbles, this becomes:

$$\mathbf{M}_{c,drag} = \frac{3}{4} \rho_c \alpha_d \frac{C_D}{d_d} \|\mathbf{v}_r\| \mathbf{v}_r, \quad (4)$$

where  $d_d$  is the bubble/particle diameter. The drag force for the dispersed phase is computed using the following property of the interphase momentum exchange:

$$\mathbf{M}_c = -\mathbf{M}_d. \quad (5)$$

In segregated flows, the interfacial shear stress term in Eqn. (2b) has a significant effect on the momentum of the fluid (Ishii and Hibiki, 2011). Given that the focus of this work is in the dispersed flow regime, this term assumed to be negligible. Additionally, in the dispersed regime, the interfacial pressure of the phases are assumed to be equal (Drew and Passman, 1998; Ishii and Hibiki, 2011) (i.e.  $P_{c,i} = P_{d,i} = P_{int}$ ) and the pressure of the dispersed phase can be approximated by the interfacial pressure ( $P_d \approx P_{d,i} = P_{int}$ ) (Ishii and Hibiki, 2011). The interfacial pressure is approximated by a volume average of the analytical solution of potential flow around a single sphere (Stuhmiller, 1977; Antal et al., 1991):

$$P_{c,i} = P_c - C_P \rho_c \mathbf{v}_r \cdot \mathbf{v}_r, \quad (6)$$

where  $C_P$  is the interfacial pressure coefficient. Thus, the momentum equations in a gas-liquid flow system is given as:

$$\begin{aligned} \frac{\partial(\alpha_l \rho_l \mathbf{v}_l)}{\partial t} + \nabla \cdot (\alpha_l \rho_l \mathbf{v}_l \mathbf{v}_l) = & -\alpha_l \nabla P_l + \nabla \cdot (\alpha_l \boldsymbol{\tau}_l) + \alpha_l \rho_l \mathbf{g} \\ & + \frac{3}{4} \alpha_g \rho_l \frac{C_D}{d_b} \|\mathbf{v}_r\| \mathbf{v}_r - C_p \mathbf{v}_r \cdot \mathbf{v}_r \nabla \alpha_l, \end{aligned} \quad (7a)$$

$$\begin{aligned} \frac{\partial(\alpha_g \rho_g \mathbf{v}_g)}{\partial t} + \nabla \cdot (\alpha_g \rho_g \mathbf{v}_g \mathbf{v}_g) = & -\alpha_g \nabla (P_l - C_p \mathbf{v}_r \cdot \mathbf{v}_r) + \nabla \cdot (\alpha_g \boldsymbol{\tau}_g) \\ & + \alpha_g \rho_g \mathbf{g} - \frac{3}{4} \alpha_g \rho_l \frac{C_D}{d_b} \|\mathbf{v}_r\| \mathbf{v}_r. \end{aligned} \quad (7b)$$

### 3. Methodology

The solid physical boundaries are imposed by blending the governing equations of the fluid with the solid Dirichlet boundary conditions. The diffuse-interface is described by the smooth function  $\phi$ , whose value is  $\pm 1$  inside the phases and is between  $(-1, 1)$  in the interface region (Shen and Yang, 2010):

$$\phi = \begin{cases} -1, & \text{fluid,} \\ 1, & \text{solid.} \end{cases} \quad (8)$$

From Eqn. (8), the governing equations of the fluid are weighted by  $(1 - \phi)/2$  to ensure that the equations are active inside the fluid. Similarly, the solid velocity boundary conditions are weighted by  $(1 + \phi)/2$  so that the conditions are inactive inside the fluid but active in the solid. The gradient of the phase-field is the normal vector from the interface and the Neumann boundary condition can be imposed using  $\mathbf{n} \approx \nabla \phi / \|\nabla \phi\|$ .

An example of this diffuse-interface approach is described using the following Poisson problem:

$$-\nabla^2 y = f \quad \text{on } \Omega, \quad \mathbf{n} \cdot \nabla y = h \quad \text{on } \Gamma_N, \quad y = g \quad \text{on } \Gamma_D. \quad (9)$$

The physical domain is denoted by  $\phi = -1$  and the area outside the physical domain by  $\phi = 1$ . The equation is then weighted by  $(1 - \phi)/2$  and the Dirichlet condition is weighted by  $(1 + \phi)/2$ :

$$\frac{1 - \phi}{2} (\nabla^2 y + f) + \frac{1 + \phi}{2} (y - g) = 0. \quad (10)$$

Taking the inner product of Eqn. (10) with the test function,  $\varphi$ :

$$\left\langle \frac{1 - \phi}{2} \nabla^2 y, \varphi \right\rangle_\Omega + \left\langle \frac{1 - \phi}{2} f, \varphi \right\rangle_\Omega + \left\langle \frac{1 + \phi}{2} (y - g), \varphi \right\rangle_\Omega = 0, \quad (11)$$

where  $\langle \cdot, \cdot \rangle$  is the inner product operator. The Neumann boundary condition is obtained by applying integration by parts to the Laplacian term:

$$\left\langle \frac{1-\phi}{2} \nabla^2 y, \varphi \right\rangle_{\Omega} = \left\langle \frac{1-\phi}{2} \mathbf{n} \cdot \nabla y, \varphi \right\rangle_{\Gamma'_N} + \left\langle \frac{1}{2} \nabla \phi \cdot \nabla y, \varphi \right\rangle_{\Omega} - \left\langle \frac{1-\phi}{2} \nabla y, \nabla \varphi \right\rangle_{\Omega}, \quad (12)$$

where  $\Gamma'_N$  is the part of the simulation domain boundary that the Neumann boundary condition applies to and  $\mathbf{n}$  is the unit normal (outward) of the surface bounding the domain. Substituting this back into Eqn. (11) and applying the Neumann boundary condition:

$$\begin{aligned} \left\langle \frac{1-\phi}{2} h, \varphi \right\rangle_{\Gamma'_N} + \left\langle \frac{1}{2} h \|\nabla \phi\|, \varphi \right\rangle_{\Omega} - \left\langle \frac{1-\phi}{2} \nabla y, \nabla \varphi \right\rangle_{\Omega} \\ + \left\langle \frac{1-\phi}{2} f, \varphi \right\rangle_{\Omega} + \left\langle \frac{1+\phi}{2} (y-g), \varphi \right\rangle_{\Omega} = 0, \end{aligned} \quad (13)$$

where the second term of the left-hand side is obtained from substituting the definition of the diffuse-interface unit normal into the Neumann boundary condition in Eqn. (9):

$$\frac{\nabla \phi}{\|\nabla \phi\|} \cdot \nabla y = h. \quad (14)$$

Equation (13) is the weak formulation of Eqn. (9) with a diffuse-interface. The Neumann boundary condition is imposed via the first and/or second terms, depending on the location of the Neumann boundary. If the Neumann boundary condition is on the simulation domain, the  $\frac{1-\phi}{2}h$  term on  $\Gamma'_N$  is used to impose the Neumann boundary condition. However, if the boundary is defined by the diffuse-interface, the  $\frac{1}{2}h\|\nabla \phi\|$  term in  $\Omega$  is used instead. In the case where the boundary condition applies on both the simulation and diffuse-interface boundaries, then both terms are used. Similarly, should the Dirichlet boundary condition also apply to parts of the simulation domain boundary, the boundary condition is applied by setting  $y = g$  on  $\Gamma'_D$ .

### 3.1. Time Discretization

Prior to delving into the diffuse-interface method for two-phase flow, the notation that will be used for the time discretization must be defined. The governing equations are solved using an adaptive second/third order semi-implicit Adams-Bashforth/Backward-Differentiation (AB/BDI23) scheme (Peyret, 2002). The third order AB/BDI3 scheme is used to estimate the local error of the second order scheme. The explicit terms in the equation are discretized using the Adams-Bashforth scheme and the time derivative is discretized using backward-differentiation (Peyret, 2002). The following notation will

be used to denote the numerator of the discretized time derivative:

$$\mathbf{v}^{*'} = a_0 \mathbf{v}^* + \sum_{j=1}^k a_j \mathbf{v}^{n+1-j}, \quad (15)$$

$$\alpha^{(n+1)'} = \sum_{j=0}^k a_j \alpha^{n+1-j}, \quad (16)$$

where  $a_j$  is a coefficient associated with backward-differentiation that will later be defined and  $k$  is the order of the method. The discretized explicit terms will be denoted as follows:

$$f^{n'} = \sum_{j=0}^{k-1} b_j f^{n-j}, \quad (17)$$

where  $b_j$  is a coefficient associated with the Adams-Bashforth scheme. The procedure to calculate  $a_j$  and  $b_j$  are outlined in Section A.

### 3.2. Diffuse-Interface for Two-Fluid Model Equations

In this study, the scaled version of governing equations presented in Section 2 are solved using the phase-bounded incremental pressure correction scheme (IPCS) (Treeratanaphitak and Abukhdeir, 2019). The scaled equations are scaled using the following dimensionless parameters:  $\tilde{\mathbf{v}} = \mathbf{v}/v_s$ ,  $\tilde{t} = t/t_s$ ,  $\tilde{\mathbf{x}} = \mathbf{x}/x_s$ ,  $\tilde{P} = (P - P_0)/P_s$ ,  $\tilde{\mathbf{g}} = \mathbf{g}/g_s$ ,  $\tilde{\nabla} = x_s \nabla$  and  $\tilde{d}_b = d_b/x_s$ . This results in the following scaled equations:

$$\begin{aligned} \frac{\partial \tilde{\mathbf{v}}_l}{\partial \tilde{t}} + \tilde{\mathbf{v}}_l \cdot \tilde{\nabla} \tilde{\mathbf{v}}_l = & -Eu_l \tilde{\nabla} \tilde{P}_l + \frac{1}{Re_l} \frac{\tilde{\nabla} \alpha_l \cdot \tilde{\boldsymbol{\tau}}_l}{\alpha_l} + \frac{1}{Re_l} \tilde{\nabla} \cdot \tilde{\boldsymbol{\tau}}_l + \frac{1}{Fr^2} \tilde{\mathbf{g}} \\ & + \frac{3}{4} \frac{\alpha_g}{\alpha_l} \frac{C_D}{\tilde{d}_b} \|\tilde{\mathbf{v}}_r\| \tilde{\mathbf{v}}_r - C_P \tilde{\mathbf{v}}_r \cdot \tilde{\mathbf{v}}_r \frac{\tilde{\nabla} \alpha_l}{\alpha_l}, \end{aligned} \quad (18a)$$

$$\begin{aligned} \frac{\partial \tilde{\mathbf{v}}_g}{\partial \tilde{t}} + \tilde{\mathbf{v}}_g \cdot \tilde{\nabla} \tilde{\mathbf{v}}_g = & -Eu_g \tilde{\nabla} \left( \tilde{P}_l - C_P \tilde{\mathbf{v}}_r \cdot \tilde{\mathbf{v}}_r \frac{\rho_l}{\rho_g} \right) + \frac{1}{Re_g} \frac{\tilde{\nabla} \alpha_g \cdot \tilde{\boldsymbol{\tau}}_g}{\alpha_g} \\ & + \frac{1}{Re_g} \tilde{\nabla} \cdot \tilde{\boldsymbol{\tau}}_g + \frac{1}{Fr^2} \tilde{\mathbf{g}} - \frac{3}{4} \frac{\rho_l}{\rho_g} \frac{C_D}{\tilde{d}_b} \|\tilde{\mathbf{v}}_r\| \tilde{\mathbf{v}}_r, \end{aligned} \quad (18b)$$

$$\frac{\partial \alpha_g}{\partial \tilde{t}} + \tilde{\nabla} \cdot (\alpha_g \tilde{\mathbf{v}}_g) = 0, \quad (18c)$$

$$\alpha_l = 1 - \alpha_g, \quad (18d)$$

where the dimensionless groups are defined in Table 1.

The diffuse solid-fluid interface is imposed by blending the governing equations of the two-fluid model (Eqn. (18)) and the solid Dirichlet boundary condition together. This is achieved by weighting the governing equations and solid boundary condition by  $(1 - \phi)/2$  and  $(1 + \phi)/2$ , respectively. The weighting allows for integrals over the

Table 1: Dimensionless groups

Parameter	Expression
Time	$t_s = v_s/x_s$
Pressure	$P_s = \rho_l g_s h$ $P_0 = 0$
Euler number	$Eu_q = P_s/\rho_q v_s^2$
Reynolds number	$Re_q = \rho_q v_s x_s/\mu_q$
Froude number	$Fr = v_s/\sqrt{g_s x_s}$

physical domain to be reformulated into volume integrals over the simulation domain (Nguyen et al., 2018). The resulting system of equations is as follow:

$$\frac{1-\phi}{2} \left( \frac{\tilde{\mathbf{v}}_q^{*'}}{\Delta t} + \tilde{\mathbf{v}}_q^{n'} \cdot \tilde{\nabla} \tilde{\mathbf{v}}_q^{n'} \right) = \frac{1-\phi}{2} \left[ \mathbf{RHS}_q^n + \frac{1}{Re_q} \frac{\tilde{\nabla} \alpha_q^{n'} \cdot \tilde{\boldsymbol{\tau}}_q^{n+1}}{\alpha_q^{n'}} \right. \\ \left. + \frac{1}{Re_q} \tilde{\nabla} \cdot \tilde{\boldsymbol{\tau}}_q^{n+1} + \frac{1}{Fr^2} \tilde{\mathbf{g}} \right] \quad \text{in } \Omega, \quad (19)$$

where:

$$\mathbf{RHS}_l^n = -Eu_l \tilde{\nabla} \tilde{P}_l^n + \frac{3}{4} \frac{\alpha_g^{n'}}{\alpha_l^{n'}} \frac{C_D}{\tilde{d}_b} \left\| \tilde{\mathbf{v}}_r^{n'} \right\| \tilde{\mathbf{v}}_r^{n'} - C_P \tilde{\mathbf{v}}_r^{n'} \cdot \tilde{\mathbf{v}}_r^{n'} \frac{\tilde{\nabla} \alpha_l^{n'}}{\alpha_l^{n'}}, \quad (20a)$$

$$\mathbf{RHS}_g^n = -Eu_g \tilde{\nabla} \left( \tilde{P}_l^n - C_P \tilde{\mathbf{v}}_r^{n'} \cdot \tilde{\mathbf{v}}_r^{n'} \frac{\rho_l}{\rho_g} \right) - \frac{3}{4} \frac{\rho_l}{\rho_g} \frac{C_D}{\tilde{d}_b} \left\| \tilde{\mathbf{v}}_r^{n'} \right\| \tilde{\mathbf{v}}_r^{n'}, \quad (20b)$$

with the following boundary conditions:

$$\frac{1+\phi}{2} \tilde{\mathbf{v}}_q^* = \mathbf{0} \quad \text{in } \Omega, \quad (21a)$$

$$\frac{1-\phi}{2} \tilde{\mathbf{v}}_q^* = \frac{1-\phi}{2} \tilde{\mathbf{v}}_{q,BC}^{n+1} \quad \text{on } \Gamma'_D, \quad (21b)$$

$$\mathbf{n} \cdot \frac{1-\phi}{2} \tilde{\boldsymbol{\tau}}_q^{n+1} = \mathbf{0} \quad \text{on } \Gamma'_N. \quad (21c)$$

The time discretization follows the notation defined in Section 3.1. The weak formulation of Eqn. (19) follows the same procedure as the Poisson equation example outlined earlier in the section but with the two-fluid model equations. Taking the inner product

of Eqn. (19) and the test function yields:

$$\begin{aligned}
& \left\langle \frac{1-\phi}{2} \frac{\tilde{\mathbf{v}}_q^{*'}}{\Delta t}, \boldsymbol{\varphi}_q \right\rangle_{\Omega} + \left\langle \frac{1+\phi}{2} \frac{a_0 \tilde{\mathbf{v}}_q^*}{\Delta t}, \boldsymbol{\varphi}_q \right\rangle_{\Omega} \\
&= - \left\langle \frac{1-\phi}{2} \tilde{\mathbf{v}}_q^{n'} \cdot \tilde{\nabla} \tilde{\mathbf{v}}_q^{n'}, \boldsymbol{\varphi}_q \right\rangle_{\Omega} + \left\langle \frac{1-\phi}{2} \mathbf{RHS}_q^n, \boldsymbol{\varphi}_q \right\rangle_{\Omega} \\
&+ \left\langle \frac{1-\phi}{2} \frac{1}{Re_q} \frac{\tilde{\nabla} \alpha_q^{n'} \cdot \tilde{\boldsymbol{\tau}}_q^{n+1}}{\alpha_q^{n'}}, \boldsymbol{\varphi}_q \right\rangle_{\Omega} + \left\langle \frac{1-\phi}{2} \frac{1}{Re_q} \tilde{\nabla} \cdot \tilde{\boldsymbol{\tau}}_q^*, \boldsymbol{\varphi}_q \right\rangle_{\Omega} \\
&+ \left\langle \frac{1-\phi}{2} \frac{1}{Fr^2} \tilde{\mathbf{g}}, \boldsymbol{\varphi}_q \right\rangle_{\Omega}.
\end{aligned} \tag{22}$$

The Neumann boundary condition for Eqn. (19) is obtained from using integration by parts on the  $\frac{1-\phi}{2} \frac{1}{Re_q} \tilde{\nabla} \cdot \tilde{\boldsymbol{\tau}}_q^*$  term:

$$\begin{aligned}
\left\langle \frac{1-\phi}{2} \frac{1}{Re_q} \tilde{\nabla} \cdot \tilde{\boldsymbol{\tau}}_q^*, \boldsymbol{\varphi}_q \right\rangle_{\Omega} &= \left\langle \frac{1-\phi}{2} \frac{1}{Re_q} \mathbf{n} \cdot \tilde{\boldsymbol{\tau}}_q^{n+1}, \boldsymbol{\varphi}_q \right\rangle_{\Gamma'_N} + \left\langle \frac{1}{2Re_q} \tilde{\nabla} \phi \cdot \tilde{\boldsymbol{\tau}}_q^*, \boldsymbol{\varphi}_q \right\rangle_{\Omega} \\
&- \left\langle \frac{1-\phi}{2} \frac{1}{Re_q} \tilde{\boldsymbol{\tau}}_q^* \cdot \tilde{\nabla} \boldsymbol{\varphi}_q \right\rangle_{\Omega}.
\end{aligned} \tag{23}$$

The second term in the right-hand side of Eqn. (23) allows for the imposition of a Neumann boundary condition at the solid-fluid interface. In this work, the boundary condition at the solid-fluid interface is a Dirichlet boundary condition and the term is therefore left unconstrained. The weak formulation is thus:

$$\begin{aligned}
& \left\langle \frac{1-\phi}{2} \frac{\tilde{\mathbf{v}}_q^{*'}}{\Delta t}, \boldsymbol{\varphi}_q \right\rangle_{\Omega} + \left\langle \frac{1+\phi}{2} \frac{a_0 \tilde{\mathbf{v}}_q^*}{\Delta t}, \boldsymbol{\varphi}_q \right\rangle_{\Omega} \\
&= - \left\langle \frac{1-\phi}{2} \tilde{\mathbf{v}}_q^{n'} \cdot \tilde{\nabla} \tilde{\mathbf{v}}_q^{n'}, \boldsymbol{\varphi}_q \right\rangle_{\Omega} + \left\langle \frac{1-\phi}{2} \mathbf{RHS}_q^n, \boldsymbol{\varphi}_q \right\rangle_{\Omega} \\
&+ \left\langle \frac{1-\phi}{2} \frac{1}{Re_q} \frac{\tilde{\nabla} \alpha_q^{n'} \cdot \tilde{\boldsymbol{\tau}}_q^{n+1}}{\alpha_q^{n'}}, \boldsymbol{\varphi}_q \right\rangle_{\Omega} + \left\langle \frac{1-\phi}{2} \frac{1}{Re_q} \mathbf{n} \cdot \tilde{\boldsymbol{\tau}}_q^{n+1}, \boldsymbol{\varphi}_q \right\rangle_{\Gamma'_N} \\
&- \left\langle \frac{1-\phi}{2} \frac{1}{Re_q} \tilde{\boldsymbol{\tau}}_q^* \cdot \tilde{\nabla} \boldsymbol{\varphi}_q \right\rangle_{\Omega} + \left\langle \frac{1-\phi}{2} \frac{1}{Fr^2} \tilde{\mathbf{g}}, \boldsymbol{\varphi}_q \right\rangle_{\Omega},
\end{aligned} \tag{24}$$

where the solid boundary condition is weighted by  $a_0/\Delta t$  for consistency. The pressure Poisson equation is derived from Eqn. (19) by taking the difference between the weighted momentum equation for  $\tilde{\mathbf{v}}_q^{n+1}$  and  $\tilde{\mathbf{v}}_q^*$  and neglecting the contributions of convection,

viscous stress and interphase momentum transfer:

$$-\tilde{\nabla} \cdot \left[ \frac{1-\phi}{2} \sum_q Eu_q \alpha_q^{n'} \tilde{\nabla} (\tilde{P}_l^{n+1} - \tilde{P}_l^n) \right] = \frac{a_0}{\Delta t} \tilde{\nabla} \cdot \left[ \frac{1-\phi}{2} \sum_q (\alpha_q^{n+1} \tilde{\mathbf{v}}_q^{n+1} - \alpha_q^n \tilde{\mathbf{v}}_q^*) \right]. \quad (25)$$

The right-hand side term can be separated into two terms:

$$\begin{aligned} \frac{a_0}{\Delta t} \tilde{\nabla} \cdot \left[ \frac{1-\phi}{2} \sum_q (\alpha_q^{n+1} \tilde{\mathbf{v}}_q^{n+1} - \alpha_q^n \tilde{\mathbf{v}}_q^*) \right] &= -\frac{a_0}{2\Delta t} \tilde{\nabla} \phi \cdot \sum_q (\alpha_q^{n+1} \tilde{\mathbf{v}}_q^{n+1} - \alpha_q^n \tilde{\mathbf{v}}_q^*) \\ &+ \frac{a_0}{\Delta t} \frac{1-\phi}{2} \tilde{\nabla} \cdot \sum_q (\alpha_q^{n+1} \tilde{\mathbf{v}}_q^{n+1} - \alpha_q^n \tilde{\mathbf{v}}_q^*). \end{aligned} \quad (26)$$

The first term is only active at the solid-fluid interface and given that the phase fraction and velocity of the solid are always known, this term is assumed to be negligible. Using the incompressibility condition for the two-fluid model,  $\nabla \cdot \sum_q \alpha_q \mathbf{v}_q = 0$ , the pressure Poisson equation for two-phase flow using the diffuse-interface method is thus:

$$\tilde{\nabla} \cdot \left[ \frac{1-\phi}{2} \sum_q Eu_q \alpha_q^{n'} \tilde{\nabla} (\tilde{P}_l^{n+1} - \tilde{P}_l^n) \right] = \frac{a_0}{\Delta t} \frac{1-\phi}{2} \tilde{\nabla} \cdot \left( \sum_q \alpha_q^n \tilde{\mathbf{v}}_q^* \right), \quad (27)$$

with the following weak formulation obtained using integration by parts:

$$\begin{aligned} \left\langle \frac{1-\phi}{2} \sum_q Eu_q \alpha_q^{n'} \mathbf{n} \cdot \tilde{\nabla} (\tilde{P}_l^{n+1} - \tilde{P}_l^n), \varphi_p \right\rangle_{\Gamma_D'} - \left\langle \frac{1-\phi}{2} \sum_q Eu_q \alpha_q^{n'} \tilde{\nabla} (\tilde{P}_l^{n+1} - \tilde{P}_l^n), \tilde{\varphi}_p \right\rangle_{\Omega} \\ = \left\langle \frac{a_0}{\Delta t} \frac{1-\phi}{2} \tilde{\nabla} \cdot \left( \sum_q \alpha_q^n \tilde{\mathbf{v}}_q^* \right), \varphi_p \right\rangle_{\Omega}. \end{aligned} \quad (28)$$

The new velocity update equation is simply sum of the update equation from IPCS weighted by  $(1-\phi)/2$  and the solid Dirichlet boundary condition weighted by  $(1+\phi)/2$ :

$$\left\langle \frac{1-\phi}{2} a_0 \frac{\tilde{\mathbf{v}}_q^{n+1} - \tilde{\mathbf{v}}_q^*}{\Delta t}, \varphi_q \right\rangle_{\Omega} + \left\langle \frac{1+\phi}{2} a_0 \frac{\tilde{\mathbf{v}}_q^{n+1}}{\Delta t}, \varphi_q \right\rangle_{\Omega} = - \left\langle \frac{1-\phi}{2} Eu_q \tilde{\nabla} (\tilde{P}_l^{n+1} - \tilde{P}_l^n), \varphi_q \right\rangle_{\Omega}. \quad (29)$$

The boundary condition for the gas fraction,  $\alpha_g$ , at the solid-fluid interface is  $\alpha_g = 0$  (liquid wets the wall). Using the same blending procedure to apply the boundary condition yields the following:

$$\left\langle \frac{1-\phi}{2} \frac{\alpha_g^{(n+1)'}}{\Delta t}, \varphi_\alpha \right\rangle_{\Omega} + \left\langle \frac{1+\phi}{2} a_0 \frac{\alpha_g^{n+1}}{\Delta t}, \varphi_\alpha \right\rangle_{\Omega} + \left\langle \frac{1-\phi}{2} \tilde{\nabla} \cdot (\alpha_g^{n+1} \tilde{\mathbf{v}}_g^{n+1}), \varphi_\alpha \right\rangle_{\Omega} = 0. \quad (30)$$

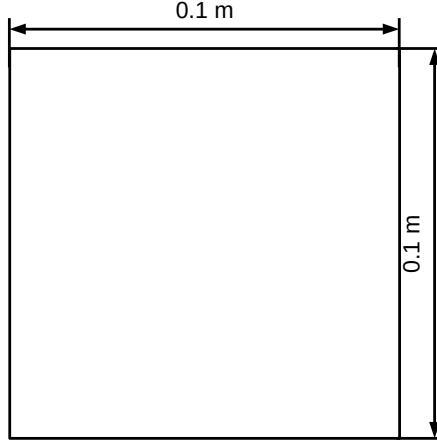


Figure 1: Simulation domain for gas-liquid flow inside a channel with the diffuse-interface method.

Table 2: Physical properties

Property	Value
Gas density ( $\text{kg/m}^3$ )	10
Liquid density ( $\text{kg/m}^3$ )	1000
Gas viscosity (Pa s)	$2 \times 10^{-5}$
Liquid viscosity (Pa s)	$5 \times 10^{-3}$
Bubble diameter (m)	$10^{-3}$
Drag constant	$\max \left[ \frac{24}{Re} (1 + 0.15 Re^{0.687}), 0.44 \right], Re = \frac{\rho_l \ \mathbf{v}_r\  d_b}{\mu_l}$

### 3.3. Simulation Conditions

The diffuse-interface method is used to impose boundary conditions in dispersed gas-liquid simulations of a two-dimensional channel (Fig. 1) and flow past a stationary cylinder (Fig. 2). The physical properties of the fluids are reported in Table 2. For the two-dimensional channel case, results from previous work by the authors (Treeratanaphitak and Abukhdeir, 2019) are used as the reference case with a conformal mesh. The width of the channel in Fig. 1 is twice that of the simulation domain in Treeratanaphitak and Abukhdeir (2019). The channel walls will be imposed using a phase-field and the remaining boundary conditions are the same as in Treeratanaphitak and Abukhdeir (2019). The new inlet boundary conditions are given in Table 3. For the case of flow past a cylinder, parabolic velocity and gas fraction profiles are used at the inlet (Table 4), no-slip and zero gas fraction conditions are imposed at the channel and cylinder walls and outflow conditions are used at the outlet.

## 4. Results and Discussion

To validate the diffuse-interface method for imposing static solid boundaries, simulations of two-phase flow using the diffuse-interface are compared to simulation results



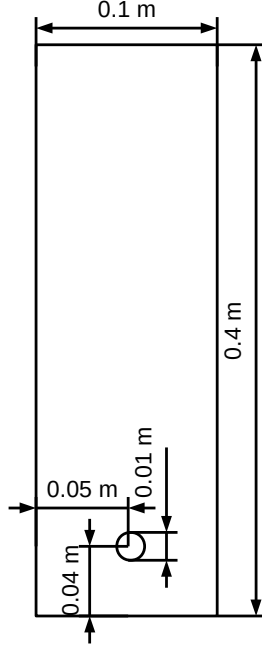


Figure 2: Simulation domain for gas-liquid flow past a stationary cylinder with the diffuse-interface method.

Table 3: Initial and inlet conditions for gas-liquid channel flow with diffuse-interface.

	Condition
Initial	$\alpha_g(\mathbf{x}, 0) = 0$ $\mathbf{v}_g(\mathbf{x}, 0) = \mathbf{v}_l(\mathbf{x}, 0) = \mathbf{0}$ $P(\mathbf{x}, 0) = \rho_l g_s(0.1 - y)$
Inlet	$\mathbf{v}_g(x, 0, t) = \left( 0, \min\left(\frac{t}{t_0}, 1\right) \frac{1-\phi}{2} 0.0616 \exp\left[-\frac{\left(\frac{x}{0.025}\right)^2}{2\sigma^2}\right] \right), t_0 = 0.625 \text{ s}, \sigma = 0.1$ $\mathbf{v}_l(x, 0, 0) = \mathbf{0}$ $\alpha_g(x, 0, t) = \min\left(\frac{t}{t_0}, 1\right) \frac{1-\phi}{2} 0.026 \exp\left[-\frac{\left(\frac{x}{0.025}\right)^2}{2\sigma^2}\right], t_0 = 0.625 \text{ s}, \sigma = 0.1$ $\mathbf{n} \cdot \frac{1-\phi}{2} \nabla (P_l(x, 0, t) - P_l(x, 0, t - \Delta t)) = 0$

Table 4: Initial and inlet conditions for gas-liquid flow past a cylinder.

	Condition
Initial	$\alpha_g(\mathbf{x}, 0) = 0$
	$\mathbf{v}_g(\mathbf{x}, 0) = \mathbf{v}_l(\mathbf{x}, 0) = \mathbf{0}$
	$P(\mathbf{x}, 0) = \rho_l g_s(0.4 - y)$
Inlet	$\mathbf{v}_g(x, 0, t) = \left(0, \min\left(\frac{t}{t_0}, 1\right)0.0616(0.025 - x^2)\right), t_0 = 0.625 \text{ s}$
	$\mathbf{v}_l(x, 0, 0) = \mathbf{0}$
	$\alpha_g(x, 0, t) = \min\left(\frac{t}{t_0}, 1\right)0.02(0.025 - x^2), t_0 = 0.625 \text{ s}$
	$\mathbf{n} \cdot \nabla P(x, 0, t) = 0$

from a boundary-conformal mesh for both channel flow and flow past a cylinder. The effect of the diffuse-interface length-scale and function type on the solution and the performance of the method are discussed.

#### 4.1. Channel Flow

The phase-field that defines the channel is described using the following hyperbolic tangent function:

$$\phi(\tilde{\mathbf{x}}) = \tanh\left(\frac{|\tilde{\mathbf{x}}| - \tilde{x}_c}{0.5\epsilon}\right), \quad (31)$$

where  $\tilde{x}_c = 0.5$  is the scaled distance from the centerline to the channel wall and  $\epsilon$  is a parameter associated with the width of the diffuse-interface. The function will asymptotically approach  $\phi = -1$  and  $\phi = 1$ , ensuring a smooth transition between the phases. The scaled width of the interface,  $\eta$ , is approximated by the distance between  $\phi = -0.999$  and  $\phi = 0.999$  which is given by  $\eta = \epsilon \tanh^{-1}(0.999)$ .

The presence of the diffuse-interface alters the way the no-slip boundary condition is imposed at the channel walls. In the case of a boundary-conformal mesh, the velocities at the walls are set to zero. However, in the diffuse-interface method, the no-slip condition is blended with the governing equations for the two-fluid model. The sharpness of the velocity gradient from the channel walls to the bulk is now a function of the diffuse-interface function, interface width and the discretization scheme.

In this study, the spatial discretization scheme is the same for all of the simulations but two different orders of the temporal discretization scheme are used to estimate the local error. The difference between near-wall velocity gradients from second-order and third-order AB/BDI methods are the largest contributor to the local error and local error tolerance of  $\epsilon_l = 10^{-4}$  resulted in very small step sizes. This issue is particularly significant in cases where the diffuse-interface is large such as in channel flow. To alleviate the constraint on the step size, only the local error inside the fluid domain, where  $\phi \leq -0.999$ , is considered when computing the new step size and the local error tolerance is relaxed to  $\epsilon_l = 10^{-3}$ .

The gas phase fraction profile at  $t = 1.72 \text{ s}$  obtained from a simulation with a diffuse-interface given by Eqn. (31) and  $\epsilon = 0.02$  is shown in Fig. 3. The profile for  $\phi$  is

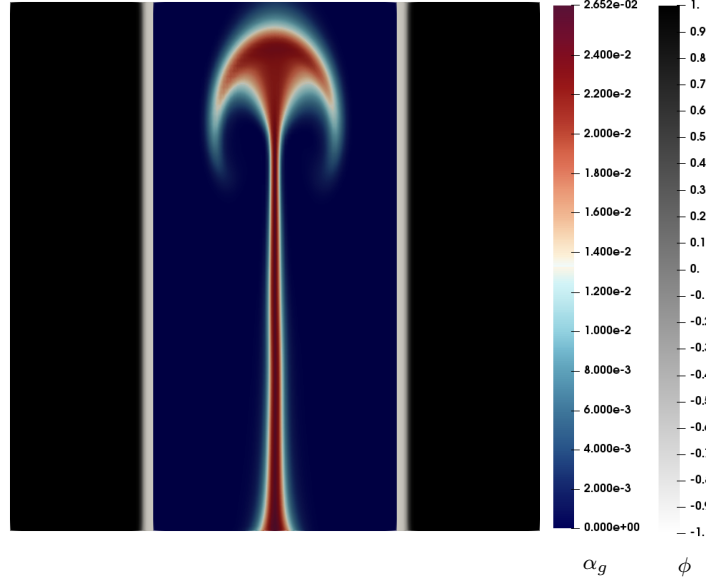


Figure 3: Surface plot of  $\alpha_g$  at  $t = 1.72$  s with hyperbolic tangent diffuse-interface and  $\epsilon = 0.02$ . The grayscale colorbar denotes the phase-field that describes the diffuse-interface, thresholded to show  $\phi \geq -0.999$ .

superimposed onto the image and thresholded to only show  $\phi \geq -0.999$ . Qualitatively, the phase fraction profile and transient behavior is in agreement to that observed in Treeratanaphitak and Abukhdeir (2019). A bubble plume is observed as the gas phase convects through the liquid phase. Over time, the plume increases in width and the vortices in the wake of the plume also increase in size. This is in agreement with experimental observations of the startup period in rectangular bubble columns (Mudde, 2005). Figure 5 shows the gas and liquid velocity streamlines inside the box given by  $x \in [-0.025, 0.025]$  and  $y \in [0, 0.1]$  at the same time step. From Figs. 4 and 5, the velocity profiles of both gas and liquid phases are similar with liquid recirculating in the wake of the bubble plume.

In addition to qualitative comparisons of the phase fraction profile and velocity streamlines, the time evolution of the gas hold-up from the diffuse-interface simulation will also be compared to that of the reference solution from Treeratanaphitak and Abukhdeir (2019). The gas hold-up in the diffuse-interface simulation is computed as follows:

$$\langle \alpha_g \rangle = \frac{\int_{\Omega} \frac{1-\phi}{2} \alpha_g d\Omega}{\int_{\Omega} \frac{1-\phi}{2} d\Omega}, \quad (32)$$

where denominator is the volume of the physical domain. This comparison is reported in the subsequent sections.

#### 4.1.1. Effect of Interface Length-Scale

The nature of the diffuse-interface can affect simulation results and how well they closely replicate the boundary-conformal mesh solutions. This section will explore the

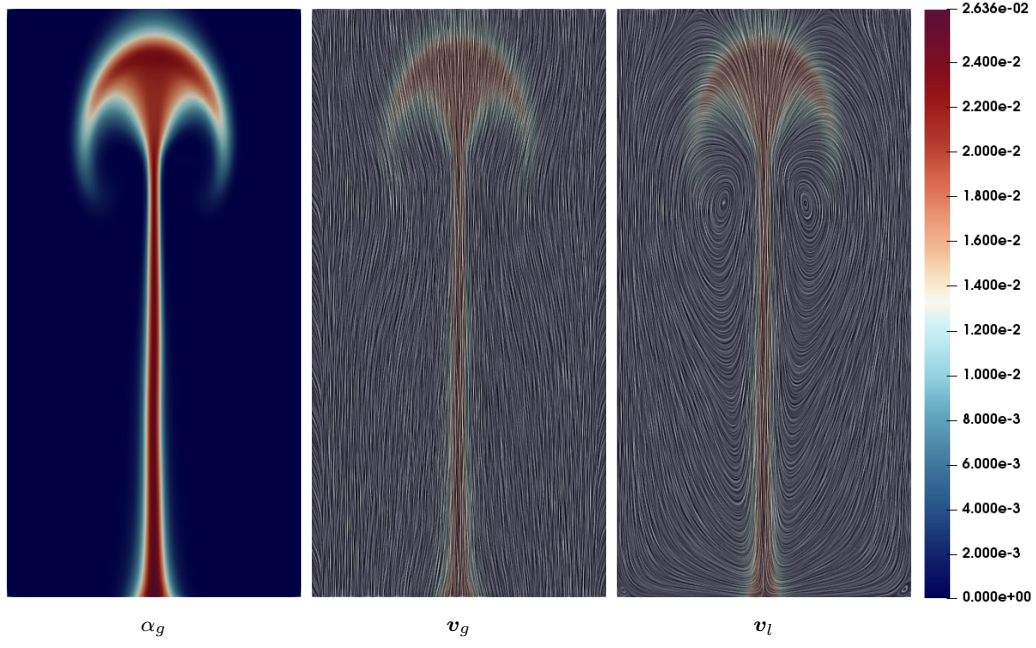


Figure 4: Surface plot of (left) phase fraction, (center) gas velocity and (right) liquid velocity at  $t = 1.72$  s from bounded IPCS with interfacial pressure. Reprinted from Treeratanaphitak and Abukhdeir (2019) with permission from Elsevier.

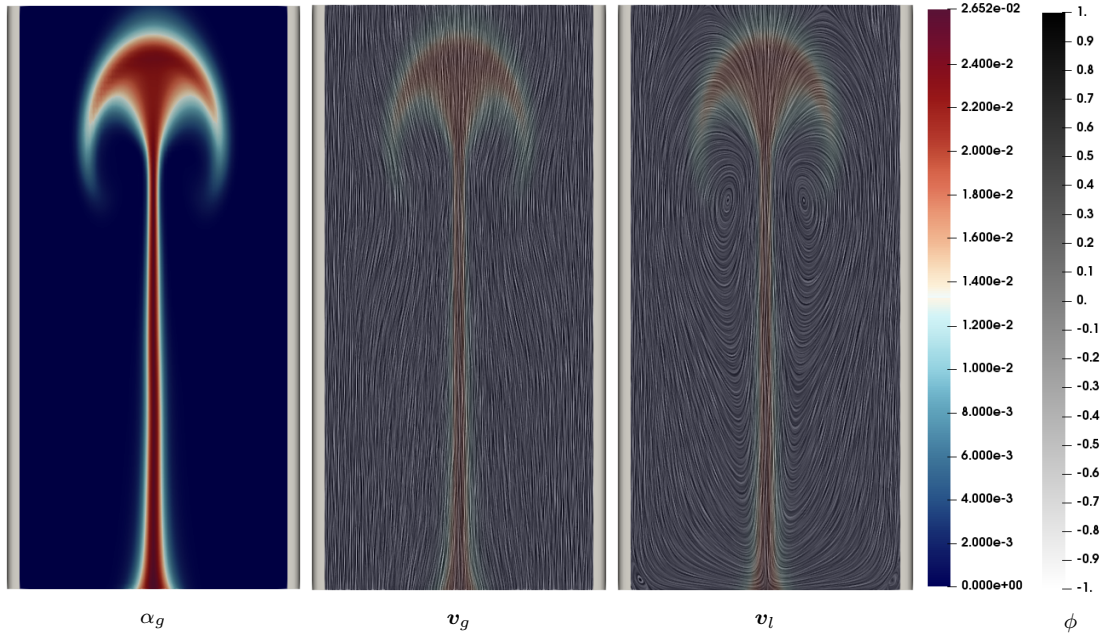


Figure 5: Surface plot of (left)  $\alpha_g$ , (center) gas velocity and (right) liquid velocity at  $t = 1.72$  s with hyperbolic tangent diffuse-interface and  $\epsilon = 0.02$ .

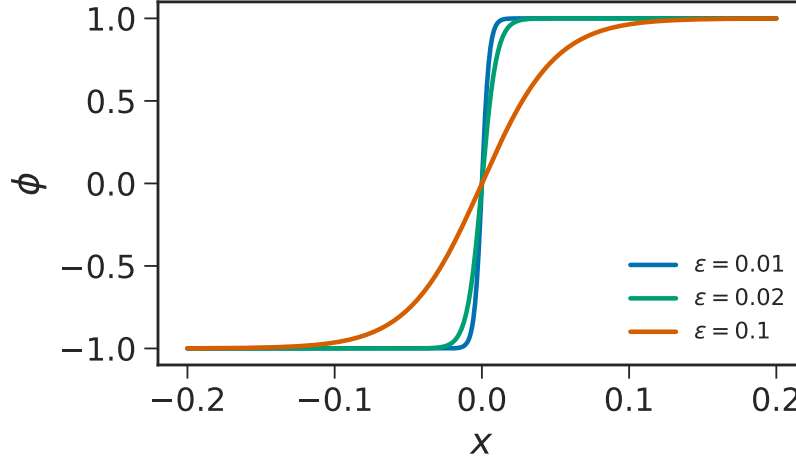


Figure 6: Comparison of diffuse-interface width generated using the same hyperbolic tangent function with varying  $\epsilon$ .

effect of interface length-scale on the solution. Simulations of the same channel flow system is repeated with  $\epsilon = 0.01, 0.02, 0.04, 0.08$  and  $0.1$ . Figure 6 shows how the  $\phi = \tanh(x/0.5\epsilon)$  profile changes with different values of  $\epsilon$ .  $\epsilon = 0.01$  corresponds to the case where the interface is sharper and  $\epsilon = 0.1$  to the case where the interface is very diffuse.

As the interface widens, the contribution of local error from blending increases. But given that this contribution is localized to the interface and that only the local error inside the fluid is considered when computing the new step size, the step size is comparable between all values of  $\epsilon$ . Figures 7 and 8 show the gas phase fraction at  $t = 1.72$  s for simulations with  $\epsilon = 0.01$  and  $\epsilon = 0.1$ , respectively. Visually, gas fraction profile from  $\epsilon = 0.01$  is nearly identical to the case with  $\epsilon = 0.02$  but the profile from  $\epsilon = 0.1$  is notably different from  $\epsilon = 0.02$ . In Fig. 8, noticeable wobbling is observed in the gas column below the plume and the plume is much narrower. This is due to the interface being very diffuse and the effect of the solid boundary conditions is smeared further into the fluid domain.

The gas and liquid velocity streamlines from  $\epsilon = 0.01$  and  $\epsilon = 0.1$  are shown in Figs. 9 and 10, respectively. The streamlines from  $\epsilon = 0.01$  are qualitatively similar to those observed in Figs. 4 and 5. However, the streamlines from  $\epsilon = 0.1$  are different from the other simulations. The gas velocity streamlines appear to exhibit less curvature in the wake of the bubble plume and the liquid velocity vortices in the wake of the plume are narrower due to the highly diffuse nature of the interface.

Figure 11 shows the time evolution of the overall gas hold-up,  $\langle \alpha_g \rangle$ , inside the channel up to 2.5 s from the hyperbolic tangent diffuse-interface simulations and the reference solution. At narrow interface widths, the evolution of the gas hold-up follows the same pattern as the reference solution, and the magnitude of the overall hold-up

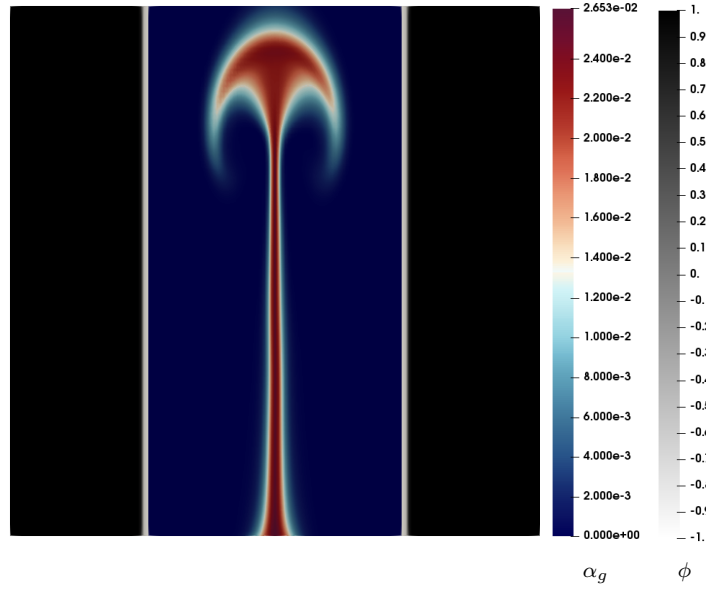


Figure 7: Surface plot of  $\alpha_g$  at  $t = 1.72$  s with hyperbolic tangent diffuse-interface and  $\epsilon = 0.01$ . The grayscale colorbar denotes the phase-field that describes the diffuse-interface, thresholded to show  $\phi \geq -0.999$ .

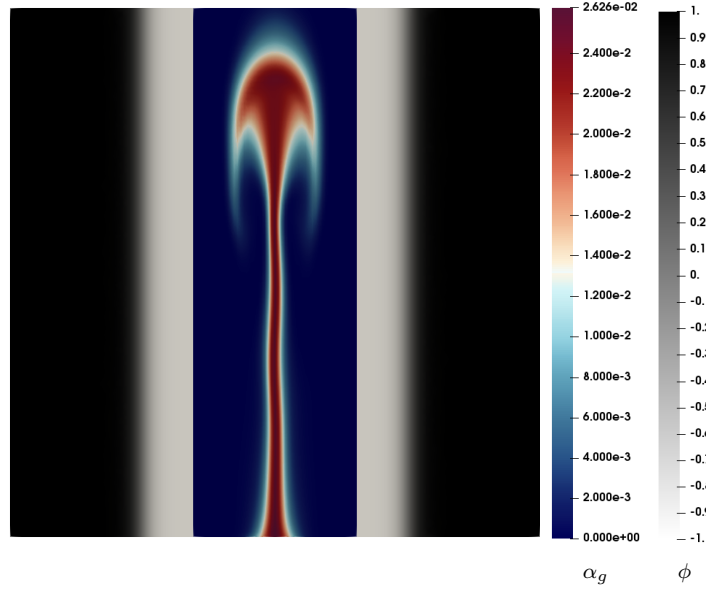


Figure 8: Surface plot of  $\alpha_g$  at  $t = 1.72$  s with hyperbolic tangent diffuse-interface and  $\epsilon = 0.1$ . The grayscale colorbar denotes the phase-field that describes the diffuse-interface, thresholded to show  $\phi \geq -0.999$ .

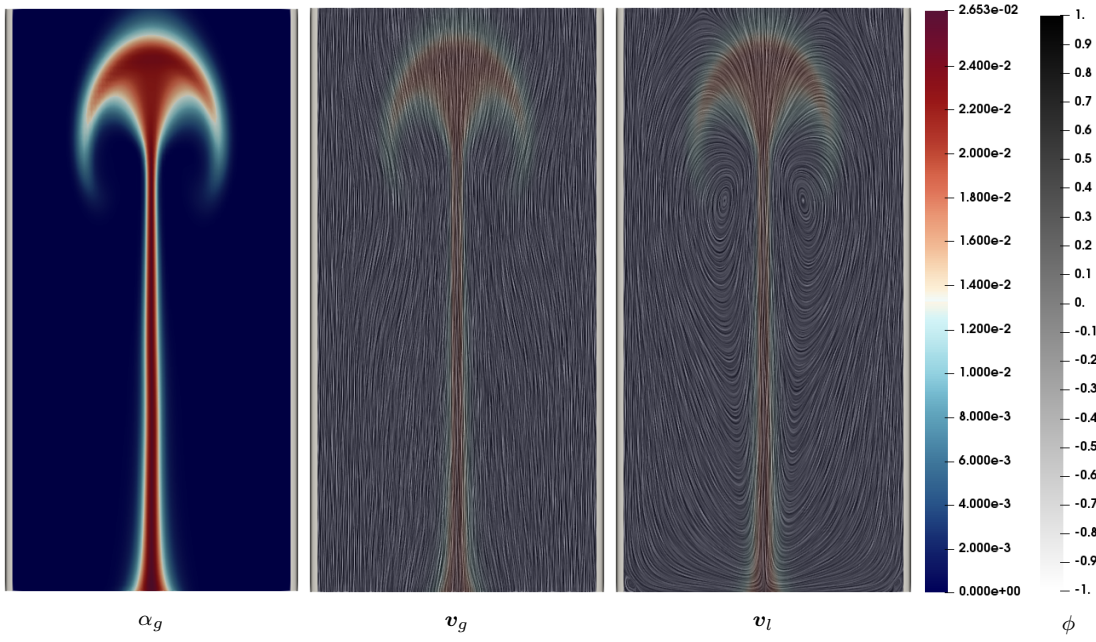


Figure 9: Surface plot of (left)  $\alpha_g$ , (center) gas velocity and (right) liquid velocity at  $t = 1.72$  s with hyperbolic tangent diffuse-interface and  $\epsilon = 0.01$ .

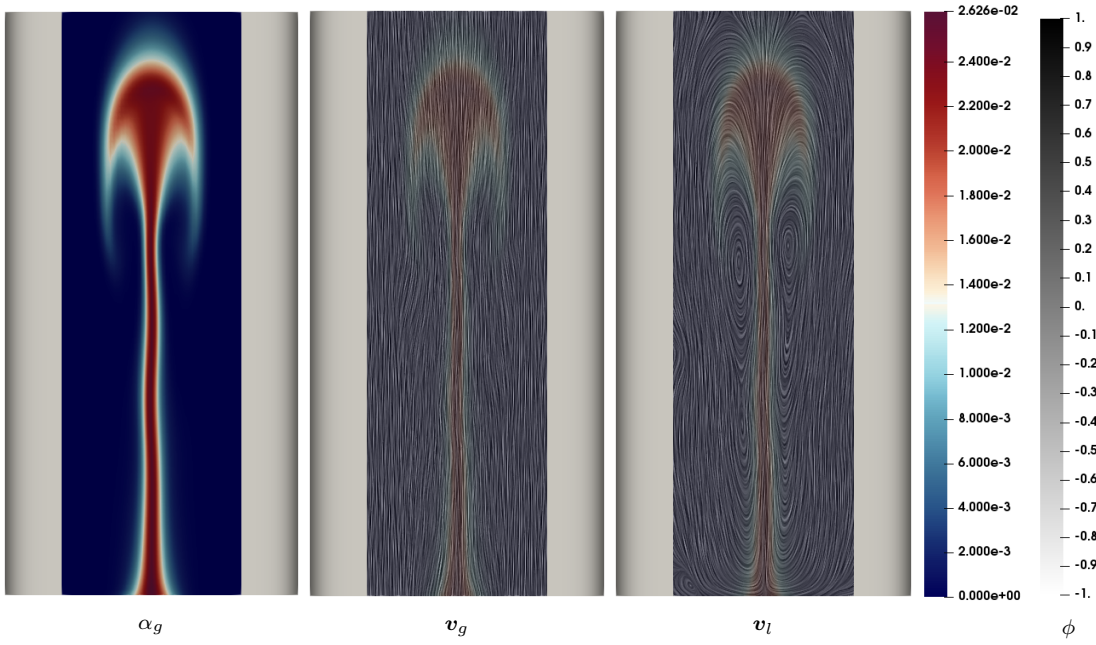


Figure 10: Surface plot of (left)  $\alpha_g$ , (center) gas velocity and (right) liquid velocity at  $t = 1.72$  s with hyperbolic tangent diffuse-interface and  $\epsilon = 0.1$ .



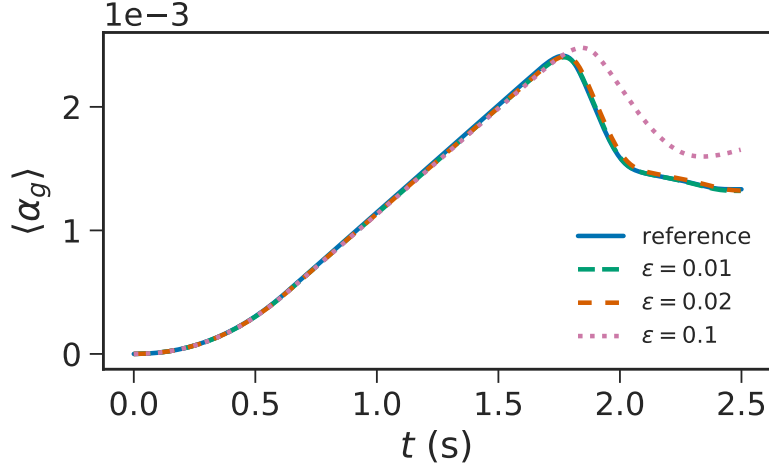


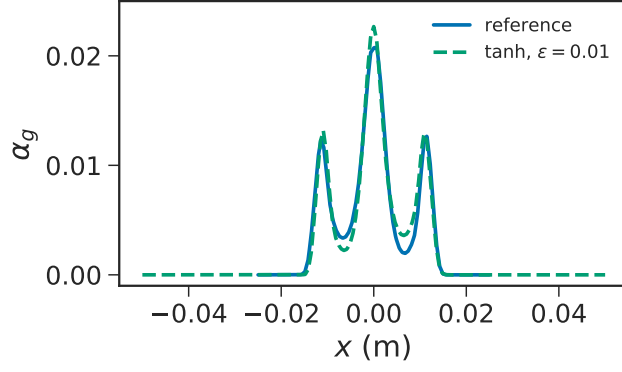
Figure 11: Time evolution of overall gas hold-up inside a channel with solid boundaries defined by a hyperbolic tangent diffuse-interface.

is almost identical. However, for  $\epsilon = 0.1$ , the evolution of the hold-up is similar to the reference solution only up to the point where the bubble plume leaves the channel. After this point, the hold-up deviates from the reference solution, indicating that the flow behavior is different. In the reference solution, the period after the bubble plume leaves the channel is where a straight vertical column of bubbly flow is observed. In the case of  $\epsilon = 0.1$ , the column of bubbly flow is not straight (Fig. 5) and the onset of precessing flow occurs much earlier than the other simulations.

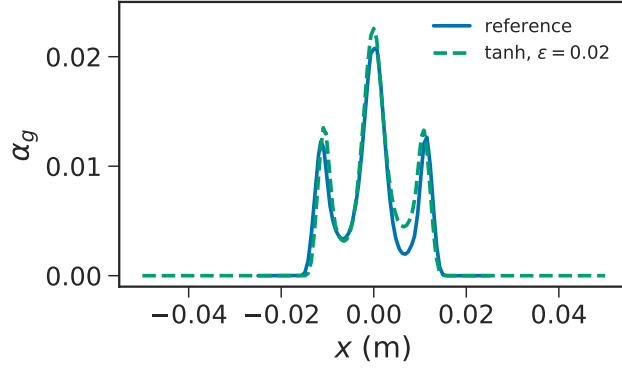
The gas fraction is sampled along the line  $y = 0.08$  m and the profile along the  $x$ -axis is plotted in Fig. 12. This height corresponds to the widest part of the bubble plume. For the cases where  $\epsilon = 0.01$  and  $\epsilon = 0.02$ , the  $\alpha_g$  profiles obtained using a diffuse-interface to impose solid boundaries show good qualitative agreement with the reference solution from Treeratanaphitak and Abukhdeir (2019). The agreement is improved as the interface becomes narrower but the difference is relatively small. As the interface becomes wider, the  $\alpha_g$  profile is no longer in agreement with the reference solution. The effect of the diffuse-interface is also clear here as  $\alpha_g$  in Fig. 12c starts to transition from  $\alpha_g = 0$  to a nonzero value further into the domain.

To obtain a quantitative measure of how the diffuse-interface simulations compare with the reference solution, the width of the bubble plume at  $y = 0.08$  m is computed and reported in Table 5. The plume widths from simulations with  $\epsilon = 0.01$  and  $\epsilon = 0.02$  are within 3% of the reference solution, supporting the observations made in this section. The plume width from  $\epsilon = 0.1$  is 30% off from the reference solution, highlighting the importance of the diffuse-interface width.

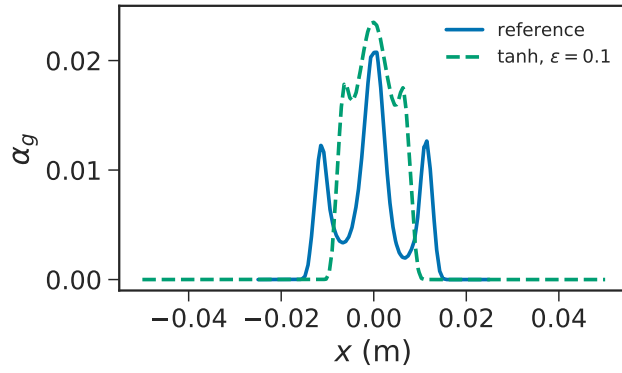




(a)  $\epsilon = 0.01$



(b)  $\epsilon = 0.02$



(c)  $\epsilon = 0.1$

Figure 12:  $\alpha_g$  profile along  $y = 0.08$  m with different hyperbolic tangent diffuse-interface widths.

Table 5: Bubble plume width at  $y = 0.08$  m from simulations using hyperbolic tangent diffuse-interface.

Study	$x_{\text{plume}} (\times 10^{-2} \text{ m})$	Difference (%)
Reference	3.21	—
$\epsilon = 0.01$	3.17	1.25
$\epsilon = 0.02$	3.12	2.80
$\epsilon = 0.04$	2.92	9.03
$\epsilon = 0.08$	2.51	21.8
$\epsilon = 0.1$	2.25	30.0

#### 4.1.2. Effect of Interface Function

The previous studies have been conducted with a hyperbolic tangent function as the phase-field. Other functions can also be used to represent the diffuse-interface as long as it ensures a smooth transition from the solid to the fluid region. An example of this is a piece-wise cosine function where the interface region is described by a cosine function that is between  $[-1, 1]$  and outside the interface region,  $\phi = \pm 1$ . Unlike the hyperbolic tangent function that asymptotically approaches the lower and upper bounds of  $\phi$ , the piece-wise cosine function will reach  $\phi = \pm 1$  exactly at the specified  $\eta$ , making it easier to control the interface width. In this section, the following piece-wise cosine function is used to impose the diffuse interface:

$$\phi(\tilde{x}) = -\cos\left(-\pi \min\left[1, \max\left(0, \frac{|\tilde{x}| - \tilde{x}_c + 0.5\eta}{\eta}\right)\right]\right), \quad (33)$$

where  $\phi$  will be  $\pm 1$  outside the region  $\tilde{x} \in (\tilde{x}_c - 0.5\eta, \tilde{x}_c + 0.5\eta)$ , depending on which side of the channel wall is  $\tilde{x}$  close to.

Figure 13 shows the how  $\phi$  varies with respect to  $x$  when defined using a hyperbolic tangent function,  $\phi = \tanh(x/0.5\epsilon)$ , and using a piece-wise cosine function centered at  $x_c = 0$ ,  $\phi = -\cos(-\pi \min[1, \max(0, (x + 0.5\eta)/\eta)])$ , for a comparable interface width. The width of the cosine interface is approximated by  $\eta = \epsilon \tanh^{-1}(0.999)$ , which corresponds to the distance between  $\phi = \pm 0.999$  in the hyperbolic tangent case. From Fig. 13, the transition of  $\phi$  from  $-1$  to  $1$  in the piece-wise cosine function is more gradual than the hyperbolic tangent function, which results in lower values of  $\nabla\phi$ .

Figure 14 shows the gas fraction profile and velocity streamlines for simulations with a piece-wise cosine diffuse-interface with a comparable interface width as the hyperbolic tangent case. At small  $\epsilon$ , the profiles are qualitatively similar to their hyperbolic tangent counterparts. The bubble plume in the  $\epsilon = 0.1$  case is still noticeably narrower than the reference solution but appears to be wider than the hyperbolic tangent result with the same  $\epsilon$ . The gas column below the plume also appears to be more stable than the results in Fig. 10.

The significant difference between the results from different interface functions at  $\epsilon = 0.1$  is due to the piece-wise nature of Eqn. (33) and the approximation of the interface width to obtain a comparable width as the asymptotic hyperbolic tangent function. In the piece-wise cosine function, the approximation  $\eta = \epsilon \tanh^{-1}(0.999)$

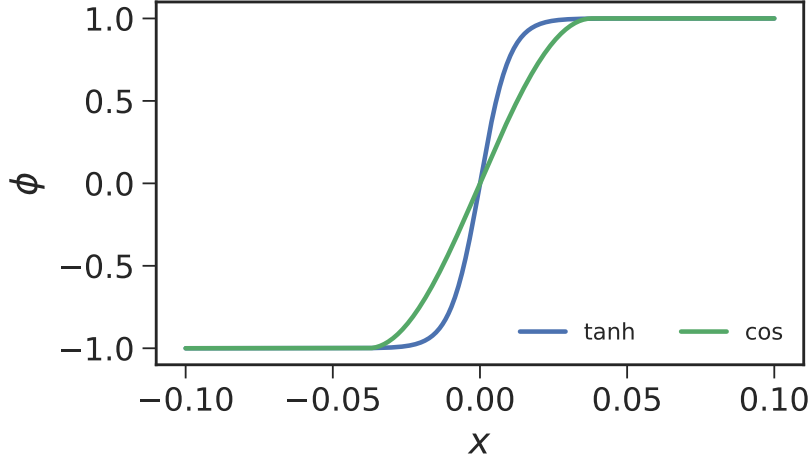


Figure 13: Comparison of diffuse-interface generated using hyperbolic tangent and piece-wise cosine functions with  $\epsilon = 0.02$  and  $\eta = \epsilon \tanh^{-1}(0.999)$ .

produces a diffuse-interface that approaches  $\phi = \pm 1$  over a similar length-scale as the hyperbolic tangent function for small interface widths. However, at  $\epsilon = 0.1$ , the difference between  $\epsilon \tanh^{-1}(0.999)$  and  $\epsilon \tanh^{-1}(0.9999)$ , which are interface widths approximated by  $\phi = \pm 0.999$  and  $\phi = \pm 0.9999$ , respectively, is an order of magnitude larger than at  $\epsilon = 0.01$  and non-negligible. The hyperbolic tangent function smears the interface over a larger distance, which for larger values of  $\epsilon$ , is detrimental to the performance of the method.

Figure 15 shows the time evolution of the overall gas-holdup for simulations with a piece-wise cosine diffuse-interface. Similar to the hyperbolic tangent case, the gas hold-up at small interface widths ( $\epsilon = 0.01$  and  $\epsilon = 0.02$ ) are in agreement with the reference solution. At  $\epsilon = 0.1$ , the gas hold-up is not in agreement with the reference solution after the bubble plume starts to exit the simulation domain but the difference is not as drastic as the hyperbolic tangent case in Fig. 11.

The  $\alpha_g$  profile at  $y = 0.08$  m from the three cases are plotted with the reference solution in Fig. 16. The results are similar to that observed in the previous section where  $\epsilon = 0.01$  and  $\epsilon = 0.02$  yielded profiles that are comparable to the reference solution but the profile from  $\epsilon = 0.1$  is different from the reference solution. Figure 17 describes the error in the phase fraction along the line  $y = 0.08$  m as the interface width varies for both interface functions. The error is defined as:

$$\text{Error} = \|\alpha_{g,ref} - \alpha_g\|_{y=0.08\text{ m}}, \quad (34)$$

and can be described using the following power-law expression:

$$\|\alpha_{g,ref} - \alpha_g\|_{y=0.08\text{ m}} = A\epsilon^m, \quad (35)$$

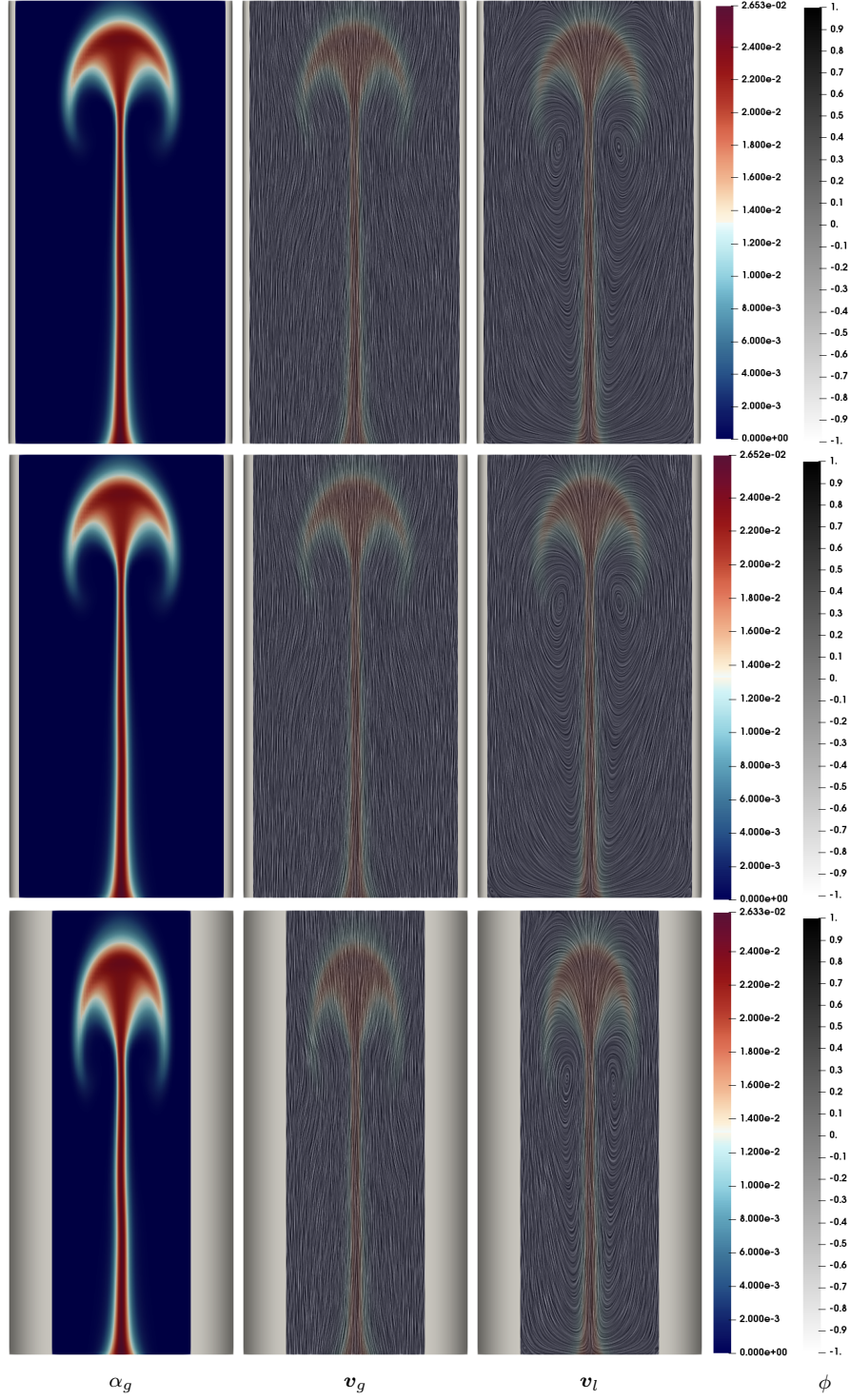


Figure 14: Surface plot of (left) phase fraction, (center) gas velocity and (right) liquid velocity at  $t = 1.72$  s with piece-wise cosine diffuse-interface and (top)  $\epsilon = 0.01$ , (middle)  $\epsilon = 0.02$  and (bottom)  $\epsilon = 0.1$ .

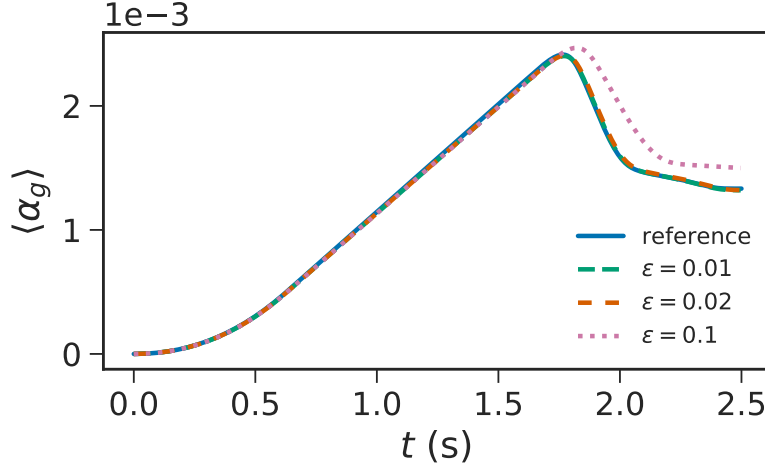


Figure 15: Time evolution of overall gas hold-up inside a channel with solid boundaries defined by a piece-wise cosine diffuse-interface.

Table 6: Bubble plume width at  $y = 0.08$  m from simulations using piece-wise cosine diffuse-interface.

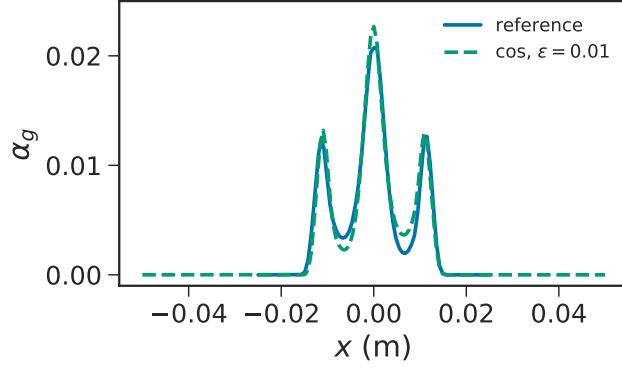
Study	$x_{\text{plume}} (\times 10^{-2} \text{ m})$	Difference (%)
Reference	3.21	—
$\epsilon = 0.01$	3.17	1.25
$\epsilon = 0.02$	3.13	2.49
$\epsilon = 0.04$	3.03	5.46
$\epsilon = 0.08$	2.75	14.2
$\epsilon = 0.1$	2.54	20.9

where  $A$  is a constant and  $m$  is the exponent. For both interface functions, the error follows an approximate first-order decay with the interface width where  $m_{\text{tanh}} = 0.953$  and  $m_{\text{cos}} = 0.896$ .

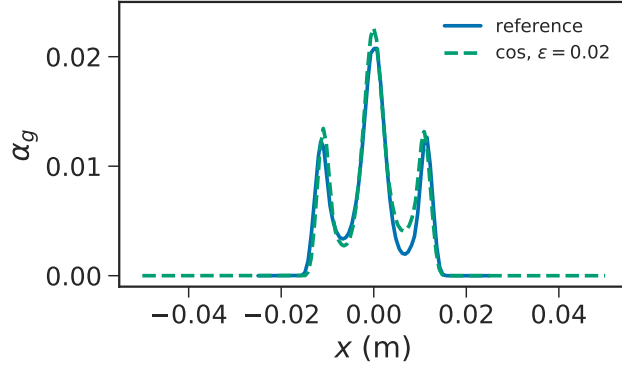
The bubble plume width is computed and tabulated in Table 6. At  $\epsilon = 0.01$ , the bubble plume width is exactly the same as the hyperbolic tangent case (Table 5). The  $\epsilon = 0.02$  yielded a small difference between the two interface functions but is still below 3%. The use of the piece-wise cosine function as the interface improved the bubble plume width in the very diffuse case, decreasing the difference from the reference solution by almost 10%. This is due to the lack of smearing when  $\phi$  is very close to  $\pm 1$  in the piece-wise cosine function compared to the hyperbolic tangent function.

#### 4.2. Flow Past a Cylinder

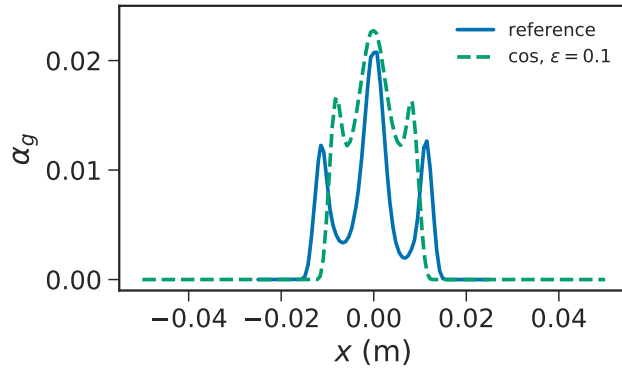
The diffuse-interface method is also used to model two-phase flow past a stationary cylinder for the first time with the two-fluid model. Simulations are performed using both the hyperbolic tangent and piece-wise cosine interface functions. For the



(a)  $\epsilon = 0.01$



(b)  $\epsilon = 0.02$



(c)  $\epsilon = 0.1$

Figure 16:  $\alpha_g$  profile along  $y = 0.08$  m with different piece-wise cosine diffuse-interface widths.

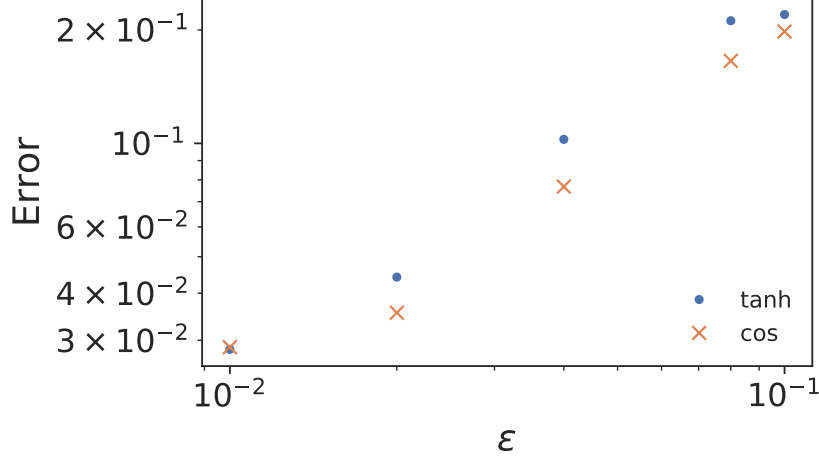


Figure 17: Error in  $\alpha_g$  profile along  $y = 0.08$  m as a function of  $\epsilon$ .

hyperbolic tangent case, the cylinder is defined using the following function:

$$\phi(\tilde{\mathbf{x}}) = -\tanh\left(\frac{\|\tilde{\mathbf{x}} - \tilde{\mathbf{x}}_c\| - \tilde{R}}{0.5\epsilon}\right), \quad (36)$$

where  $\tilde{\mathbf{x}}_c = (0, 0.8)$  is the scaled diffuse-interface position vector that corresponds to the center of the cylinder,  $\tilde{R} = 0.1$  is the scaled radius of the cylinder and  $\epsilon = 0.01$ . The piece-wise cosine interface is defined by:

$$\phi(\tilde{\mathbf{x}}) = -\cos\left(-\pi \min\left[1, \max\left(0, \frac{\|\tilde{\mathbf{x}} - \tilde{\mathbf{x}}_c\| - \tilde{R} + 0.5\eta}{\eta}\right)\right]\right), \quad (37)$$

where  $\eta = \epsilon \tanh^{-1}(0.999)$ . In this system, the presence of the diffuse-interface is expected to have a larger impact on the flow profile due to the fact that the cylinder is directly in the path of the flow. The diffuse-interface will smear the solid boundary, making the cylinder appear slightly larger than if the boundary was defined using the mesh, which in turn will affect the hydrodynamical behavior of the fluid.

Figure 18 shows the gas and liquid velocity streamlines along with the gas fraction profile from the reference solution. The reference solution is obtained from performing a simulation with the conditions outlined in Section 3.3 using a boundary-conformal mesh. In the early stages of the simulation, gas moves around the cylinder, leaving a small area behind the cylinder for liquid recirculation. Unlike flow through a rectangular channel, gas recirculation is also present in the region near the cylinder. As the gas travels further up the channel ( $t = 3.13$  s), it merges behind the cylinder and moves up the channel. There are two zones of liquid recirculation near the inlet, one on each side of the bubbly mixture. The recirculation zones grow in size and their centers move upward

( $t = 3.13$  s). Over time, more and more mixing occurs, resulting in a wavy column of bubbly mixture and a distorted bubble plume at the very top. Several recirculation zones are present on either side of the wavy column where gas is occasionally pulled into the vortex, resulting in areas of higher gas fractions.

Figures 19 and 20 show the results at the same time steps from simulations using a hyperbolic tangent and piece-wise cosine diffuse-interfaces with  $\epsilon = 0.01$ , respectively. The results do not appear to significantly differ when different interface functions are used. At  $t = 3.13$  s, the gas phase fraction profile and the velocity streamlines appear to be the same as the results from the reference simulation for both interface functions. This is not the case starting at  $t = 4.69$  s onward. The recirculation zones in the wake of the cylinder predicted by the diffuse-interface simulations are wider and closer to the cylinder. The recirculation zones around the cylinder also appear to be less distorted when compared to the reference case. This appears to have affected the evolution of the gas and velocity profiles, resulting in similar features but different gas fraction and velocity profiles, confirming the prediction made earlier in this section.

The time evolution of the overall gas hold-up is shown in Fig. 21. In the early stages of the simulation, the hold-up evolves in the same manner as the reference solution. The interface function does not appear to significantly affect the solution at  $\epsilon = 0.01$ , supporting the results from Section 4.1.2. But as the diffuse-interface interacts with the flow, the gas hold-up diverges from the reference solution. This corresponds to the observations made in Figs. 18 to 20. While the magnitude and the slope of the gas hold-up profiles from the diffuse-interface simulations vary from the reference solution, the qualitative behavior is still the same.

## 5. Conclusions

A diffuse-interface method for imposing solid boundaries in two-phase flow has been developed. The Dirichlet solid boundary conditions are imposed by blending the governing equations of the two-fluid model with the Dirichlet boundary condition, resulting in a smooth transition from the solid boundary to the fluid domain. To validate the method, simulations of channel flow and flow past a cylinder are performed and the results are compared to results from simulations with boundary-conformal meshes. The results from the diffuse-interface method for simulations of channel flow are found to be in agreement with the reference solution when the diffuse-interface is sufficiently small. At small interface widths, the choice of the interface function does not affect the accuracy of the solution. When the interface is large, the solution is negatively affected. In two-phase flow past a stationary cylinder, the results from the diffuse-interface simulations are in agreement with the reference solution in the early stages of the simulation. As the flow interacts with the cylinder, the diffuse-interface is found to affect the flow profile and the overall gas hold-up. Similar flow features are still observed but at different locations and with different magnitudes.



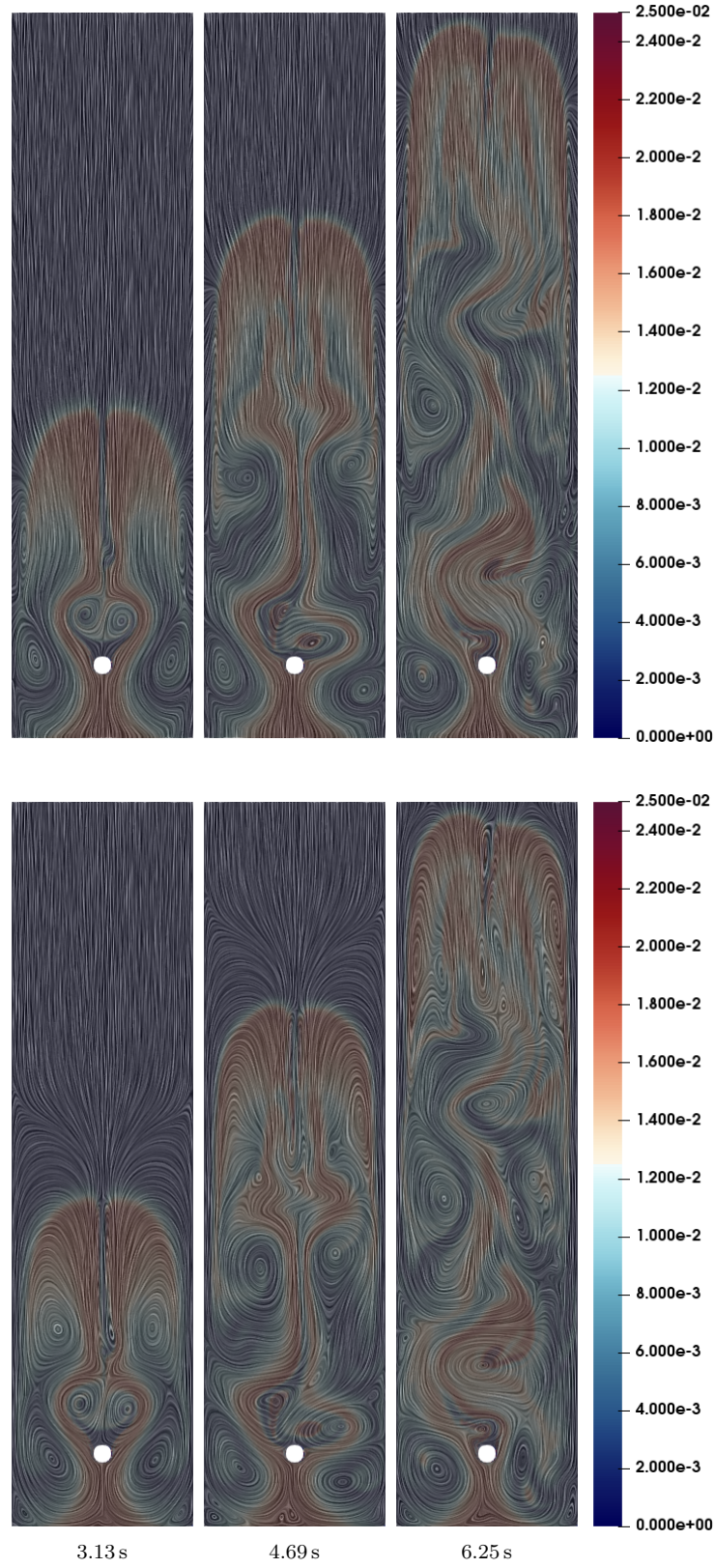


Figure 18: Evolution of gas-liquid flow past a stationary cylinder with a boundary-conformal mesh. Streamlines are of (top) gas and (bottom) liquid phases.

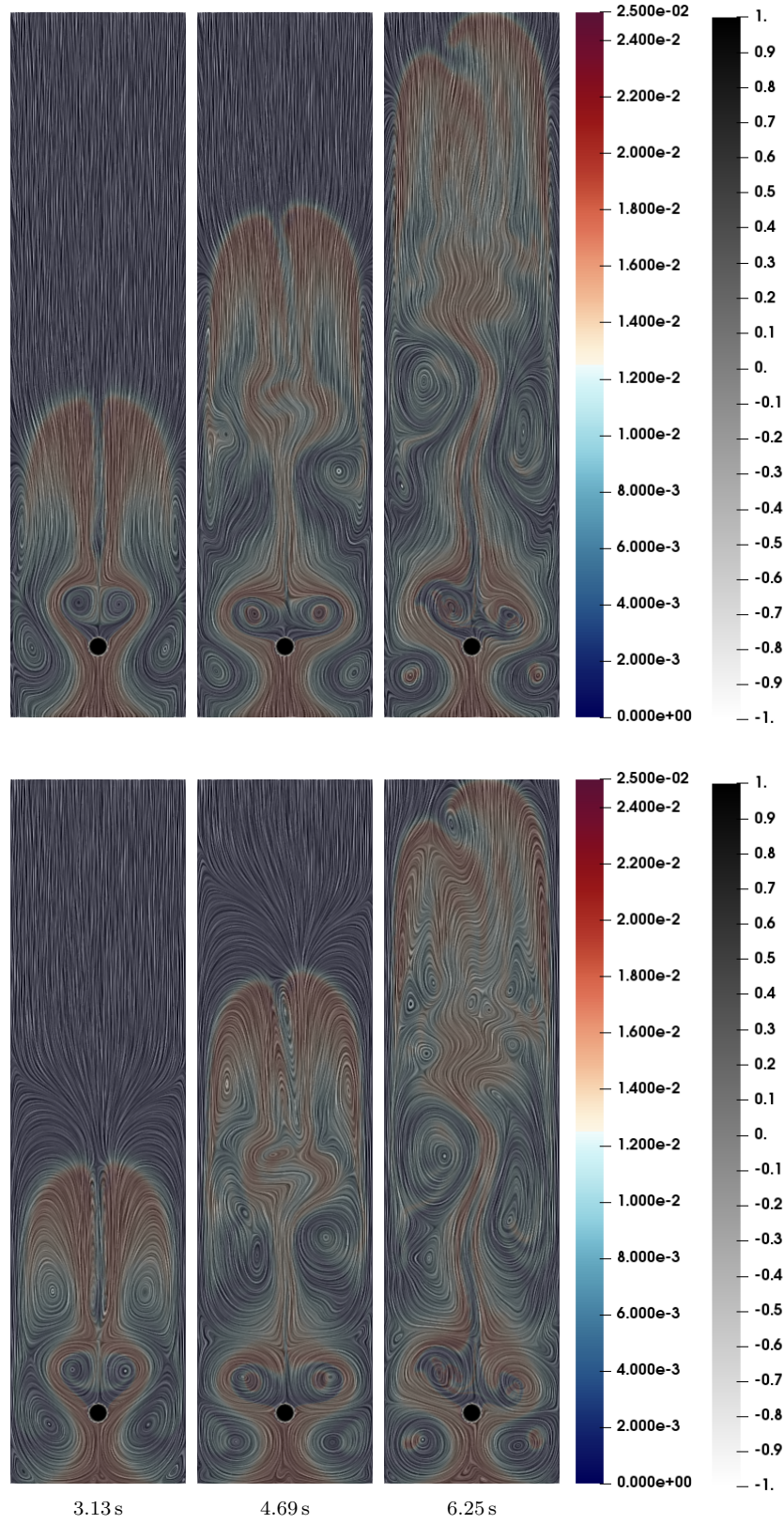


Figure 19: Evolution of gas-liquid flow past a stationary cylinder with a hyperbolic tangent diffuse-interface and  $\epsilon = 0.01$ . The diffuse-interface is in grayscale and streamlines are of (top) gas and (bottom) liquid velocities.



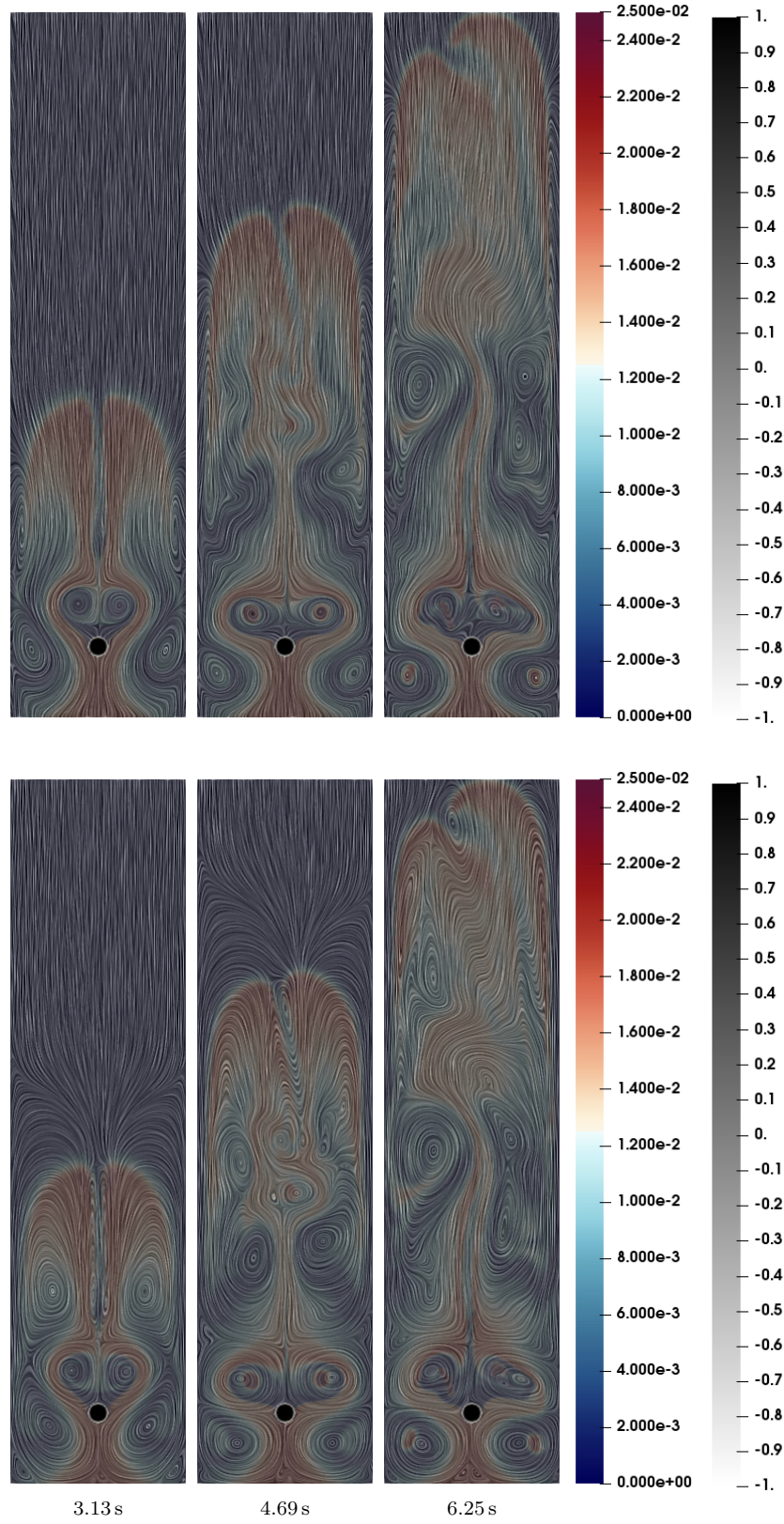


Figure 20: Evolution of gas-liquid flow past a stationary cylinder with a piece-wise cosine diffuse-interface and  $\epsilon = 0.01$ . The diffuse-interface is in grayscale and streamlines are of (top) gas and (bottom) liquid velocities.

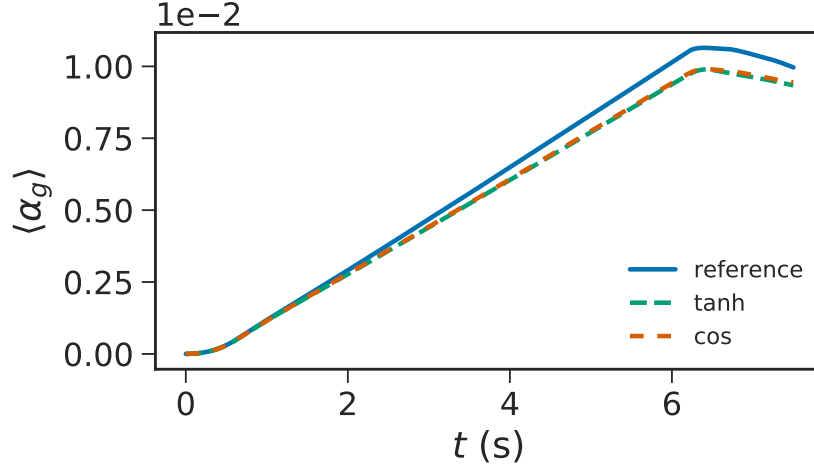


Figure 21: Time evolution of overall gas hold-up in flow past a stationary cylinder.

## Acknowledgments

This research was supported by the Natural Sciences and Engineering Research Council (NSERC) of Canada and Compute Canada.

## A. Variable Step Size Coefficients

To account for the variable step size, the coefficients  $a_j$  and  $b_j$  are functions of the previous time steps. This has the benefit of not having to interpolate between time steps to obtain the solution at  $t^n - \Delta t$  and  $t^n - 2\Delta t$ . Let  $r$  be the ratio of the previous step size to the current step size:

$$r^n = \frac{t^n - t^{n-1}}{\Delta t}, \quad (38)$$

where  $t^n - t^{n-1}$  is the step size used in the previous time step. The coefficients in AB/BDI2 can then be written in terms of  $r^n$  (Peyret, 2002):

$$a_0 = \frac{2 + r^n}{1 + r^n}, \quad a_1 = -1 - \frac{1}{r^n}, \quad a_2 = \frac{1}{r^n(1 + r^n)}, \quad (39)$$

$$b_0 = -a_1, \quad b_1 = 1 + a_1. \quad (40)$$

The same can be done for AB/BDI3 where  $r^{n-1} = (t^{n-1} - t^{n-2})/\Delta t$  (Peyret, 2002):

$$\begin{aligned} a_0 &= 1 + \frac{1}{1+r^n} + \frac{1}{1+r^n+r^{n-1}}, \\ a_1 &= -\frac{(1+r^n)(1+r^n+r^{n-1})}{r^n(r^n+r^{n-1})}, \\ a_2 &= \frac{1+r^n+r^{n-1}}{r^n r^{n-1}(1+r^n)}, \end{aligned} \tag{41}$$

$$\begin{aligned} a_3 &= -\frac{1+r^n}{r^{n-1}(r^n+r^{n-1})(1+r^n+r^{n-1})}, \\ b_0 &= -a_1, \\ b_1 &= -a_2(1+r^n), \\ b_2 &= -a_3(1+r^n+r^{n-1}). \end{aligned} \tag{42}$$

## References

- Abels, H., Garcke, H., Grün, G., 2012. Thermodynamically consistent, frame indifferent diffuse interface models for incompressible two-phase flows with different densities. *Mathematical Models and Methods in Applied Sciences* 22, 1150013. doi:10.1142/S0218202511500138.
- Abels, H., Garcke, H., Grün, G., Metzger, S., 2017. Diffuse Interface Models for Incompressible Two-Phase Flows with Different Densities. Springer International Publishing. chapter 8. pp. 203–229. doi:10.1007/978-3-319-56602-3.
- Aland, S., Lowengrub, J., Voigt, A., 2010. Two-phase flow in complex geometries: A diffuse domain approach. *Comput. Model Eng. Sci.* 57, 77–106. doi:10.3970/cmesci.2010.057.077.
- Anderson, D.M., McFadden, G.B., Wheeler, A.A., 1998. Diffuse-interface methods in fluid mechanics. *Annu. Rev. Fluid Mech.* 30, 139–165. doi:10.1146/annurev.fluid.30.1.139.
- Antal, S.P., Lahey Jr., R.T., Flaherty, J.E., 1991. Analysis of phase distribution in fully developed laminar bubbly two-phase flow. *Int. J. Multiphase Flow* 17, 635–652. doi:10.1016/0301-9322(91)90029-3.
- Arienti, M., Sussman, M., 2014. An embedded level set method for sharp-interface multiphase simulations of diesel injectors. *Int. J. Multiphase Flow* 59, 1–14. doi:10.1016/j.ijmultiphaseflow.2013.10.005.
- Becker, S., Sokolichin, A., Eigenberger, G., 1994. Gas-liquid flow in bubble columns and loop reactors: Part II. comparison of detailed experiments and flow simulations. *Chem. Eng. Sci.* 49, 5747–5762. doi:10.1016/0009-2509(94)00290-8.

- Ding, H., Spelt, P.D.M., Shu, C., 2007. Diffuse interface model for incompressible two-phase flows with large density ratios. *J. Comput. Phys.* 226, 2078–2095. doi:10.1016/j.jcp.2007.06.028.
- Donea, J., Huerta, A., Ponthot, J., Rodríguez-Ferran, A., 2004. Arbitrary Lagrangian–Eulerian Methods. American Cancer Society. chapter 14. doi:10.1002/0470091355.ecm009.
- Drew, D.A., Passman, S.L., 1998. Theory of Multicomponent Fluids. volume 135 of *Applied Mathematical Sciences*. Springer, New York.
- Ekambara, K., Dhotre, M.T., Joshi, J.B., 2005. CFD simulations of bubble column reactors: 1D, 2D and 3D approach. *Chem. Eng. Sci.* 60, 6733–6746. doi:10.1016/j.ces.2005.05.047.
- Glowinski, R., Pan, T.W., Hesla, T., Joseph, D., 1999. A distributed Lagrange multiplier/fictitious domain method for particulate flows. *Int. J. Multiphase Flow* 25, 755 – 794. doi:10.1016/S0301-9322(98)00048-2.
- Griffith, B.E., Patankar, N.A., 2020. Immersed methods for fluid-structure interaction. *Annu. Rev. Fluid Mech.* 52, 421–448. doi:10.1146/annurev-fluid-010719-060228.
- Gsell, S., Bonometti, T., Astruc, D., 2016. A coupled volume-of-fluid/immersed-boundary method for the study of propagating waves over complex-shaped bottom: Application to the solitary wave. *Comput. Fluids* 131, 56–65. doi:10.1016/j.compfluid.2016.03.013.
- Horgue, P., Prat, M., Quintard, M., 2014. A penalization technique applied to the “volume-of-fluid” method: Wettability condition on immersed boundaries. *Comput. Fluids* 100, 255–266. doi:10.1016/j.compfluid.2014.05.027.
- Ishii, M., Hibiki, T., 2011. Thermo-Fluid Dynamics of Two-Phase Flow. 2nd ed ed., Springer. doi:10.1007/978-1-4419-7985-8.
- Jacqmin, D., 1999. Calculation of two-phase Navier-Stokes flows using phase-field modeling. *J. Comput. Phys.* 155, 96–127. doi:10.1006/jcph.1999.6332.
- Jakobsen, H.A., Lindborg, H., Dorao, C.A., 2005. Modeling of bubble column reactors: Progress and limitations. *Ind. Eng. Chem. Res.* 44, 5107–5151. doi:10.1021/ie049447x.
- Joshi, J., 2001. Computational flow modelling and design of bubble column reactors. *Chem. Eng. Sci.* 56, 5893–5933. doi:10.1016/S0009-2509(01)00273-1. proceedings of the 5th International Conference on Gas-Liquid and Gas-Liquid-Solid Reactor Engineering.

- Krishna, R., van Baten, J., 2001. Scaling up bubble column reactors with the aid of CFD. *Chem. Eng. Res. Des.* 79, 283–309. doi:10.1205/026387601750281815.
- Lahey Jr., R.T., Drew, D.A., 2001. The analysis of two-phase flow and heat transfer using a multidimensional, four field, two-fluid model. *Nucl. Eng. Des.* 204, 29–44. doi:10.1016/S0029-5493(00)00337-X.
- Lane, C.D., McKnight, C.A., Wiens, J., Reid, K., Donaldson, A.A., 2016. Parametric analysis of internal gas separation within an ebullated bed reactor. *Chem. Eng. Res. Des.* 105, 44–54. doi:10.1016/j.cherd.2015.10.043.
- Li, X., Lowengrub, J., Rätz, A., Voigt, A., 2009. Solving PDEs in complex geometries: A diffuse domain approach. *Commun. Math. Sci.* 7, 81–107. doi:10.4310/CMS.2009.v7.n1.a4.
- Liu, C., Shen, J., Yang, X., 2015. Decoupled energy stable schemes for a phase-field model of two-phase incompressible flows with variable density. *J. Sci. Comput.* 62, 601–622. doi:10.1007/s10915-014-9867-4.
- Mittal, R., Iaccarino, G., 2005. Immersed boundary methods. *Annu. Rev. Fluid Mech.* 37, 239–261. doi:10.1146/annurev.fluid.37.061903.175743.
- Mudde, R.F., 2005. Gravity-driven bubbly flows. *Annu. Rev. Fluid Mech.* 37, 393–423. doi:10.1146/annurev.fluid.37.061903.175803.
- Nguyen, L.H., Stoter, S.K., Ruess, M., Sanchez Uribe, M.A., Schillinger, D., 2018. The diffuse Nitsche method: Dirichlet constraints on phase-field boundaries. *Int. J. Numer. Meth. Eng* 113, 601–633. doi:10.1002/nme.5628.
- Patel, H.V., Das, S., Kuipers, J.A.M., Padding, J.T., Peters, E.A.J.F., 2017. A coupled volume of fluid and immersed boundary method for simulating 3D multiphase flows with contact line dynamics in complex geometries. *Chem. Eng. Sci.* 166, 28–41. doi:10.1016/j.ces.2017.03.012.
- Patel, J.K., Natarajan, G., 2018. Diffuse interface immersed boundary method for multi-fluid flows with arbitrarily moving rigid bodies. *J. Comput. Phys.* 360, 202 – 228. doi:10.1016/j.jcp.2018.01.024.
- Peyret, R., 2002. Spectral Methods for Incompressible Viscous Flow. volume 148 of *Applied Mathematical Sciences*. Springer-Verlag New York.
- Ramière, I., Angot, P., Belliard, M., 2007. A fictitious domain approach with spread interface for elliptic problems with general boundary conditions. *Comput. Methods Appl. Mech. Engrg.* 196, 766–781. doi:10.1016/j.cma.2006.05.012.
- Schlottbom, M., 2016. Error analysis of a diffuse interface method for elliptic problems with Dirichlet boundary conditions. *Appl. Numer. Math.* 109, 109–122. doi:10.1016/j.apnum.2016.06.005.

- Shen, J., Yang, X., 2010. A phase-field model and its numerical approximation for two-phase incompressible flows with different densities and viscosities. *SIAM J. Sci. Comput.* 32, 1159–1179. doi:10.1137/09075860X.
- Shen, L., Chan, E.S., 2008. Numerical simulation of fluid-structure interaction using a combined volume of fluid and immersed boundary method. *Ocean Eng.* 35, 939–952. doi:10.1016/j.oceaneng.2008.01.013.
- Shen, L., Chan, E.S., 2010. Application of a combined IB-VOF model to wave–structure interactions. *Appl. Ocean Res.* 32, 40–48. doi:10.1016/j.apor.2010.05.002.
- Shen, L., Chan, E.S., 2011. Numerical simulation of nonlinear dispersive waves propagating over a submerged bar by IB-VOF model. *Ocean Eng.* 38, 319–328. doi:10.1016/j.oceaneng.2010.11.014.
- Sokolichin, A., Eigenberger, G., 1994. Gas-liquid flow in bubble columns and loop reactors: Part I. detailed modelling and numerical simulation. *Chem. Eng. Sci.* 49, 5735–5746. doi:10.1016/0009-2509(94)00289-4.
- Son, G., 2005. A level set method for incompressible two-fluid flows with immersed solid boundaries. *Numer. Heat Tr. B-Fund.* 47, 473–489. doi:10.1080/10407790590919252.
- Sotiropoulos, F., Yang, X., 2014. Immersed boundary methods for simulating fluid–structure interaction. *Prog. Aerosp. Sci.* 65, 1 – 21. doi:10.1016/j.paerosci.2013.09.003.
- Stuhmiller, J.H., 1977. The influence of interfacial pressure forces on the character of two-phase flow model equations. *Int. J. Multiphase Flow* 3, 551 – 560. doi:10.1016/0301-9322(77)90029-5.
- Suh, Y., Son, G., 2009. A sharp-interface level-set method for simulation of a piezoelectric inkjet process. *Numer. Heat Tr. B-Fund.* 55, 295–312. doi:10.1080/10407790902724552.
- Sun, X., Sakai, M., 2015. Three-dimensional simulation of gas-solid-liquid flows using the DEM-VOF method. *Chem. Eng. Sci.* 134, 531–548. doi:10.1016/j.ces.2015.05.059.
- Sun, Y., Beckermann, C., 2007. Sharp interface tracking using the phase-field equation. *J. Comput. Phys.* 220, 626–653. doi:10.1016/j.jcp.2006.05.025.
- Takada, N., Misawa, M., Tomiyama, A., 2006. A phase-field method for interface-tracking simulation of two-phase flows. *Math. Comput. Simulat.* 72, 220–226. doi:10.1016/j.matcom.2006.05.006. discrete Simulation of Fluid Dynamics in Complex Systems.



- Treeratanaphitak, T., Abukhdeir, N.M., 2019. Phase-bounded finite element method for two-fluid incompressible flow systems. *Int. J. Multiphase Flow* 117, 1–13. doi:10.1016/j.ijmultiphaseflow.2019.04.024.
- Vincent, S., Sarthou, A., Caltagirone, J.P., Sonilhac, F., Février, P., Mignot, C., Pianet, G., 2011. Augmented Lagrangian and penalty methods for the simulation of two-phase flows interacting with moving solids. application to hydroplaning flows interacting with real tire tread patterns. *J. Comput. Phys.* 230, 956–983. doi:10.1016/j.jcp.2010.10.006.
- Washino, K., Tan, H.S., Salman, A.D., Hounslow, M.J., 2011. Direct numerical simulation of solid-liquid-gas three-phase flow: Fluid-solid interaction. *Powder Technol.* 206, 161–169. doi:10.1016/j.powtec.2010.07.015.
- Weller, H., 2005. Derivation, Modelling and Solution of the Conditionally Averaged Two-Phase Flow Equations. Technical Report. Technical Report TR/HGW/02, Nabla Ltd.
- Yang, J., Stern, F., 2009. Sharp interface immersed-boundary/level-set method for wave-body interactions. *J. Comput. Phys.* 228, 6590–6616. doi:10.1016/j.jcp.2009.05.047.
- Zhang, C., Lin, N., Tang, Y., Zhao, C., 2014. A sharp interface immersed boundary/VOF model coupled with wave generating and absorbing options for wave-structure interaction. *Comput. Fluids* 89, 214–231. doi:10.1016/j.compfluid.2013.11.004.
- Zhang, C., Zhang, W., Lin, N., Tang, Y., Zhao, C., Gu, J., Lin, W., Chen, X., Qiu, A., 2013. A two-phase flow model coupling with volume of fluid and immersed boundary methods for free surface and moving structure problems. *Ocean Eng.* 74, 107–127. doi:10.1016/j.oceaneng.2013.09.010.